Master's thesis

NTNU
Norwegian University of Science and Technology
Faculty of Natural Sciences
Department of Physics

Herman Solstrand

Characterization of TiO2 based thin films using Raman spectroscopy

Master's thesis in Applied Physics
Supervisor: Turid Reenaas
Co-supervisor: Hogne Lysne
December 2021

NTNU
Norwegian University of
Science and Technology

Herman Solstrand

Characterization of TiO2 based thin films using Raman spectroscopy

Master's thesis in Applied Physics
Supervisor: Turid Reenaas
Co-supervisor: Hogne Lysne
December 2021

Norwegian University of Science and Technology
Faculty of Natural Sciences
Department of Physics

NTNU
Norwegian University of
Science and Technology

NTNU
Kunnskap for en bedre verden

Department of Physics

TFY4900 - Physics, Master's Thesis

Characterization of TiO_2 based thin films using Raman spectroscopy

Author:
Herman Solstrand

20th December 2021

Abstract

The structural characteristics of various TiO_2 based thin film samples were studied using Raman spectroscopy. The samples were deposited on 2" silicon wafer substrates using pulsed laser deposition (PLD), and some were co-doped with Cr-N, to create a potential intermediate band in the band gap of TiO_2. Not all thin film samples were grown to be uniform across the area of the substrate, and have been categorised as either "*plume samples*" (static substrate, deposited film representing the deposition plasma plume), "*film samples*" (rotating substrate, aiming to deposit a uniform film) or "*combinatorial samples*" (different plumes deposited at specific positions on the substrate, to obtain a specific concentration and/or thickness gradient across the thin film). All samples were made by Thomas Vågenes Brakstad and Hogne Lysne as part of their PhD research.

The aim of this master project was to study how the growth conditions of these films affect their crystallinity, as well as how these characteristics vary across the films, to better link any observed variations to the different depositing parameters.

The results obtained through Raman spectroscopy showed that the deposition parameters largely affect the crystallinity of TiO_2 in the deposited thin film. Both deposition with the background gas cycling between O_2 and N_2 and doping was found to severely damage the crystallinity of the deposited films, resulting in amorphous structures with broadened Raman peaks. Most thin films deposited only with a TiO_2 target and O_2 background pressure did however reveal spectra that can be attributed to the anatase phase of crystalline TiO_2.

Other factor that varied within the crystalline films, like film thickness and distance from deposition plume centre, had less of an impact on the crystallinity of the films. Both these factors did however cause variations in strain across the films, causing shifts in the Raman peaks.

For the films containing amorphous structures, the obtained Raman spectra proved more difficult to analyse in detail, and the exact structure of these films remain undetermined. Still, the Raman technique did prove to be useful, as the discovery of the amorphousness of these samples provide useful information in itself.

Preface

This project was supervised by Turid Reenaas, professor in energy and environmental physics at the Department of Physics at the Norwegian University of Science and Technology (NTNU).

The basis of this project was to study samples that were provided by Thomas Vågenes Brakstad and Hogne Lysne.

The author would like to give thanks to all the people mentioned above for their guidance and mentoring along the course of this project.

Special thanks go to Hogne Lysne and Turid Reenaas for their contributions to the sections 3.1 and 4.1 in the final text. These sections explain the principles of conventional and combinatorial PLD, and give insight about the simulation and fabrication process of the thin film samples that were studied during this present work.

Previous work

The present master work is a continuation of the authors preceding specialization project work [1]. Even though the present work is focusing on Raman spectroscopy while the specialization project was based on surface measurements using atomic force microscopy (AFM), both projects were based around characterisation work that was conducted on similar and some of the same samples. Thus, a lot of the motivation and theoretical background will overlap between these two projects, and the author therefor chose to reuse and rework some of the material from the preceding specialization project in this present master thesis for completeness. This will be the case for chapter 1 and sections 2.1, 2.2, 3.1 and 4.1.

Table of Contents

1 Introduction

The following section was reworked from the author's preceding specialization project [1]:

Solar cell technology has come a long way since the first practical silicon solar cell was publicly demonstrated at Bell Laboratories in 1954 [2], and as our need for sustainable energy production grows, photovoltaic technologies are more relevant than ever. During the evolution of photovoltaic technology, different approaches to solar cell production have come along. Still, *crystalline silicon* (c-Si) dominate the solar cell market, as this technology is well researched and established in industry and production, and has had a stable decrease in production cost and increase in efficiency [3].

There is still a clear motivation for new, high efficiency solar cell technologies, mainly for applications where the available area is restricted, and efficiency need to be at a maximum. Some of these technologies are commercially available, like *tandem cells* (though these are still very expensive and mainly used in satellite applications). Other technologies are still emerging, like *hot carrier cells*, *impact ionization cells* and *intermediate band solar cells* (IBSCs)[4]. As these technologies mature, it is also anticipated that they will eventually replace the traditional c-Si solar cells as their production cost reach a point where it is commercially competitive.

The Department of Physics at the Norwegian University of Science and Technology (NTNU) have a research team that focuses on IBSCs and the present work represent a tiny piece in this larger puzzle of IBSC research. This technology and the production and characterization of potential IB materials will therefor be the motivation of this master thesis. The highest performing IBSCs as of today have been made with both toxic and non-abundant materials, and motivated by the fact that solar cells are supposed to be a sustainable energy alternative, the presented research have focused on titanium dioxide (TiO_2) co-doped with chromium and nitrogen (Cr-N) as a potential IB material, as these are abundant, non-toxic materials. TiO_2 is also a well researched material because of its wide range of photo-electrical applications.

The samples studied during this master work consist of these TiO_2 based thin films that were grown using pulsed laser deposition (PLD). Some of these TiO_2 thin films were, as mentioned, co-doped with Cr-N, to create a potential intermediate band in the band gap of TiO_2. The samples were made by Thomas Vågenes Brakstad and Hogne Lysne as part of their PhD research, and have been divided into the following categories:

- *Plume samples* - films deposited with a single target on a stationary substrate . The resulting films thus represent a 2D projection of the deposition plasma plume, hence the name of this sample category.
- *Film samples* - centrosymmetric, flat films deposited with a single target on a rotating substrate. These films were aimed to be as uniform as possible, closer to the traditional definition of a thin film.

- *Combinatorial samples* - different plumes deposited at specific positions on the substrate, to obtain a specific concentration and/or thickness gradient across the thin film.

The aim of the author's preceding specialization project[1] was to study and characterize the surface of some of these metal oxide films using atomic force microscopy (AFM), as the obtained surface data, especially the measured roughness, can be compared to the data obtained from ellipsometry and the optical models, and give valuable insight to the quality of the thin films grown.

The work presented in this present master thesis is a continuation of the characterisation of these thin film samples. Here, Raman spectroscopy was used to further characterise the crystallinity and structure of these samples, to gain further knowledge about the samples and insight about the growth process. The list of samples studied was however not identical to that of the author's preceding specialization project[1], as the different characterisation technique led to different samples to be deemed as most interesting and prioritised for measurement.

Neither the presented work, nor the affiliated PhD research, aimed to integrate these films in an actual solar cell application. IBSC technology is still the scientific, laboratory scale context of and motivation behind the present work, and was therefore deemed worth mentioning. The scope of this thesis will however be towards material science and applied physics.

The outline of this thesis will be as follows:

In the following chapter **2**, the reader will be provided with a theoretical overview of IBSCs, thin film growth mechanisms, Raman scattering, and some material details relevant for the production of the thin film samples that were studied.

The experimental methods and techniques relevant for the present work will be presented in chapter **3**. Here, PLD and Raman spectroscopy will be presented, and the working principles of these techniques will be explained on a general basis.

In chapter **4**, the reader will be presented with the experimental details and setup behind the fabrication of the samples studied during this present work and the characterisation of these samples, using both techniques presented in chapter **3**. The reader will also be provided with some insight behind the analysis of the obtained data and the software and techniques used for this analysis. The aim of this chapter is in other words to walk the reader through the entire process, from the fabrication of the samples to the analysis of the data from the characterisation of the sample, with an overview of the experimental procedure and relevant parameters along the way.

In chapter **5**, the results obtained during the work on this present thesis will be presented, as well as analysis and discussion of the presented data. Towards the end of this chapter, the reader will also be provided with an overview of the major results and knowledge acquired from the obtained data.

The conclusions are found in chapter **6**, presenting a summary of the results presented in chapter **5** and how it ties in with the motivation stated as part of this introduction.

2 Theory

This chapter aims to provide the reader with a theoretical overview of the concepts relevant to this project, to better understand the samples and results that will be presented later.

Firstly, a brief explanation of **intermediate band solar cells** will be presented, followed by a review of **thin film growth mechanisms**, the effect of **Raman scattering** and an overview of some **material details**, to give the reader an understanding of the relevant materials, and the physics behind the fabrication and characterisation of the present samples.

2.1 Intermediate band solar cells (IBSCs)

The following section was reworked from the author's preceding specialization project [1]:

Most traditional solar cells are based on a single p-n junction, which has a theoretical maximum efficiency (η) of around 33.7 %, from the light provided by one sun, or around 40.8 % when exposed to fully concentrated light, given by the **Shockley–Queisser limit** [5]. This limit can be overcome by utilizing solar cells with multiple band gaps, increasing this theoretical limit to $\eta = 68.7$ % for normal sunlight, or $\eta = 86.8$ % using concentrated sunlight [6]. There are several ways of designing solar cells with multiple band gaps and reach these higher efficiencies. One approach is to produce multiple layered traditional solar cells (*tandem cells*), though this can be expensive in an industrial setting. As mentioned during the introduction, another solution can be to create solar cells from new materials that contain multiple band gaps within themselves; so-called *intermediate band solar cells* (IBSCs).

IBSCs contain multiple band gaps by utilizing materials with intermediate bands located within the total band gap of the material, hence the name. This allows the IBSCs to absorb sub-band gap photons, increasing the theoretical efficiency of the solar cell [7]. There are several ways of fabricating IB materials that are proposed, and different approaches to IBSC technology. One approach is through doping of semiconductor materials with specific high-density dopants, leading to the formation of an IB deep in the band gap of the pure semiconductor; so-called deep level states. Specifically *co-doping* of materials have been proposed to generate these deep level IB materials [8, 9, 10]. This entails doping a semiconductor material with a dopant pair, and differs from traditional *n-* or *p-mono-doping*, which is based on different materials and smaller doping quantities and used to create traditional *p-n junction* based solar cells. Co-doping was the approach attempted for the samples studied in this thesis, in an attempt to realize a sustainable IB material.

IBSC technology is in itself beyond the scope of this master thesis, and will thus not be explained in any further detail.

2.2 Thin film growth mechanisms

The following section was taken from the author's preceding specialization project and included for completeness [1]:

The properties of a thin film is largely connected to its structure, which is governed by the different growth parameters and growth conditions during its deposition. The formation of thin films is a process that schematically starts with **nucleation** followed by **coalescence** and subsequent **thickness growth**, all stages of which can be influenced by deposition parameters [11]. Most thin film deposition techniques operate at thermodynamic equilibrium, though there are techniques where this is not the case, as will be explained later during this section. This initial description of thin film growth will however assume that the conditions are at or near thermodynamic equilibrium.

As for all phase transitions, the formation of thin films is characterized by the formation of nuclei and their growth (**nucleation**). Depending on the interaction energies of substrate atoms and film atoms, any of three growth modes can occur [11]:

- *Layer by layer* - In the two-dimensional Frank–van der Merwe mode, layers of material grow one on top of another. Interaction between substrate and film atoms is greater than between adjacent film atoms.
- *Island* - In the Volmer–Weber mode, separate three-dimensional islands form on the substrate. Interaction between film atoms is greater than between adjacent film and substrate atoms.
- *Layer plus island* - In the Stranski–Krastanov mode, one or two monolayers form first, followed by individual islands.

The next stage of three-dimensional film formation is the growth of islands until they touch one another to form a continuous network. This so-called **coalescence** process is extremely important for the design of films with special properties. After solidlike coalescence of two islands there may remain a grain boundary between them, or they may fuse together in a liquidlike fashion to form a new, larger, and boundary-free island.

Following is the stage of **thickness growth**, where the structure still depend on the following processes [11]:

- *Shadowing* - A geometric interaction between the arriving admolecules and the roughness of the growing surface. This effect is dominant at low substrate temperatures T_S. It occurs because the vapor beam is directed.
- *Surface diffusion* - Mobility of admolecules at surfaces and interfaces such as grain boundaries; dominant at medium substrate temperatures T_S.
- *Bulk diffusion* - Mobility of admolecules in the volume of grains; dominant at high T_S.

- *Recrystallization* - Phase transition as a complete change of crystal orientation; dominant at percolation thickness, large film thickness, and high T_S.

Introducing defects to the thin film generally can also have a major influence on the physical properties of the solid, for instance, on the transmission of light and on electrical conductivity [11]. Defects can be introduced through doping of the deposited material.

One technique for thin film growth that deviates from the description above is pulsed laser deposition (PLD), which was the basis for the fabrication of the samples studied during this project. PLD differs from most other thin film deposition techniques because it does not operate at or near thermodynamic equilibrium, as the thin film material is deposited at much higher kinetic energy than with conventional deposition techniques, and with extremely high instantaneous deposition rates. The film properties may be strongly influenced by the high deposition rates, and materials with properties that are not obtainable in thermal equilibrium can be obtained. Other factors than the ones mentioned earlier in this section will thus affect the thin film growth, like laser intensity, background gas environment, what material is deposited and substrate temperature and structure. With PLD, it is therefor possible to fabricate thin films with less defects than most thin films and crystallinity comparable to that of bulk mono-crystals. The PLD technique will be further explained in section 3.1.

After the films are deposited, there are many ways of studying their structure and characteristics. Raman spectroscopy can be used to study the crystallinity and chemical composition of a thin film, and is the characterisation technique that was used during the present project. To understand this technique we fist need to understand the effect of Raman scattering:

2.3 Raman scattering

Raman scattering, first discovered by Indian scientist C. V. Raman et al. in 1928 [12], is *inelastic* scattering of photons by matter through the interaction with molecular vibrations. This is opposed to **Rayleigh scattering**, which is the phenomena that occurs when light or other electromagnetic radiation is *elastically* scattered by particles much smaller than the wavelength of the radiation [13]. Most light scatters elastically, and Rayleigh scattering usually has an intensity in the range 0.1 % to 0.01 % relative to that of a radiation source. However a tiny fraction of the light (approximately 1 part in 10 million) can be scattered inelastically as Raman scattered photons, with the scattered photons having a different energy from those of the incident photons. Where energy is lost the Raman scattering is designated as *Stokes*, and where energy is gained the Raman scattering is designated as *anti-Stokes* [14]. Typically Raman scattering involves vibrational energy being gained by a molecule (i.e. creating a phonon), as incident photons from a visible laser are shifted to lower energy, i.e. "normal" Stokes Raman scattering. An overview of the differences between the two types of Raman scattering and Rayleigh scattering is shown in figure 2.1 [15].

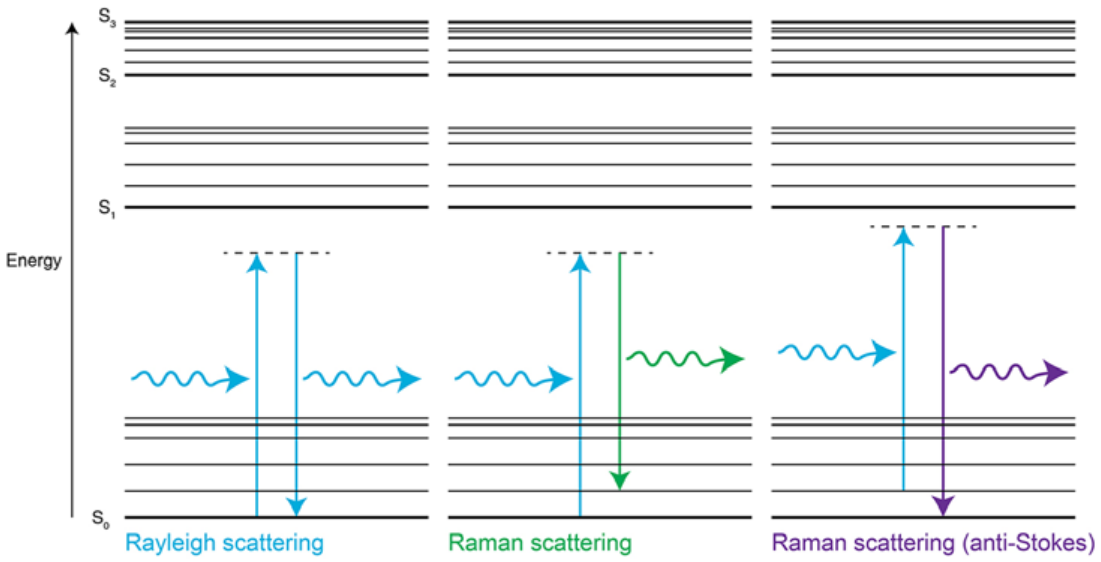

Figure 2.1: Rayleigh and Raman scattering energy diagram. S_0, S_1, S_2 are electronic energy levels, with higher energy vibrational levels. [15]

This change in light energy through Raman scattering is dependant on the *frequency of vibration* of the scattering molecule. If it is very fast (high frequency), from light atoms held together with strong bonds, the energy change is significant. If it is very slow (low frequency), from heavy atoms held together with weak bonds, the energy change is small [15]. These different vibrational frequencies arrive from what is referred to as the *vibrational modes* of the material, each responsible for a characteristic energy change, or *Raman shift* of the incident light.

For solids, and especially crystals, these vibrational modes are associated with the creation or annihilation of *phonons*, which is the quantum unit of the energy of a lattice vibration [14], similar to the way a photon represents a quantum of energy proportional to the radiation frequency of light or other electromagnetic radiation. Thus, the vibrational modes of solids are often referred to as *phonon modes* or *phononic modes*. It is worth mentioning that Raman scattering similarly can occur through emission or absorption of *magnons* (spin waves) [14], though this will not be discussed in his thesis.

Almost all materials exhibit Raman scattering. The only exception is pure metals, as they just reflect light. A change in polarisability is required during the vibration of the molecules for the Raman effect to occur and metals do not exhibit this polarisability change [15]. Carbides, nitrides and oxides do however Raman scatter. Single molecules in e.g. a gas can also scatter light through *rotational* Raman scattering, which together with the more prominent Rayleigh scattering actually contributes to the appearance of the blue sky [13]. This is however not relevant for this project, and will not be discussed any further, as the focus of this project is Raman scattering in solids and crystals.

When studying crystalline solids, the structure of the crystal lattice will give rise to these different, characteristic vibrational modes, which in turn will cause different characteristic Raman shifts in the incident light. By using a radiation source with a

single colour (wavelength) of light, like a laser, one can measure these shifts caused by the Raman scattering. As the shift is characteristic of the species present in the sample, the effect of Raman scattering is exploited by chemists and physicists to gain information about materials for a variety of purposes by performing various forms of *Raman spectroscopy*, as will be explained further in chapter 3.2.

2.4 Material details

In this section, to give a better understanding of the thin films that were studied in this master project, the reader is provided with an overview of the relevant materials that were used as target materials during deposition. The materials in question are TiO_2, which was the basis of most of the deposited thin films, and CrN, which is the material that was used as target material for the co-doping of some of these TiO_2 thin films. Some thin films only deposited using CrN will also be studied, and will serve as material for reference and discussion when analysing the doped TiO_2 thin film that was studied during this master project.

As the Raman spectrum of a thin film is linked to its crystal structure, knowledge of the possible crystal structures of these materials is necessary to understand and analyse the obtained Raman data.

2.4.1 Titanium dioxide (TiO_2)

Titanium dioxide (TiO_2) is a wide band gap semiconductor, and has been the subject of much research due to its potential photo-electrical applications [8]. The TiO_2 group is composed of the minerals *anatase*, *rutile* and *brookite*, each with different crystal structures and optical properties. In bulk form, the rutile phase of TiO_2 is more stable than its anatase phase, whereas brookite is highly unstable [16]. Therefore, we mainly expect to observe rutile and anatase in our samples.

Figure 2.2 [17] shows the different crystal structures of TiO_2, with anatase and rutile both having a tetragonal structure and brookite an orthorhombic structure. The differences in structures will lead to different vibrational modes and thus also different Raman spectra. This makes it possible to distinguish the different crystal structures of TiO_2 using Raman spectroscopy, even though they all have the same chemical composition and stoichiometry.

2.4.2 Magnéli phases (Ti_nO_{2n-1})

The homologous titanium oxide series Ti_nO_{2n-1} ($n \geq 4$) are known as the *Magnéli phases* [18]. The crystal structure of these mixed-valence compounds consists of successive rutile blocks separated by crystallographic shear planes. A sufficient oxygen vacancy in rutile TiO_2 is known to create these compounds, and they may thus be obtained from reduction of TiO_2 at a high temperature, leading to a lamellar crystalline structure which is supposed to induce solid lubricant properties similar to

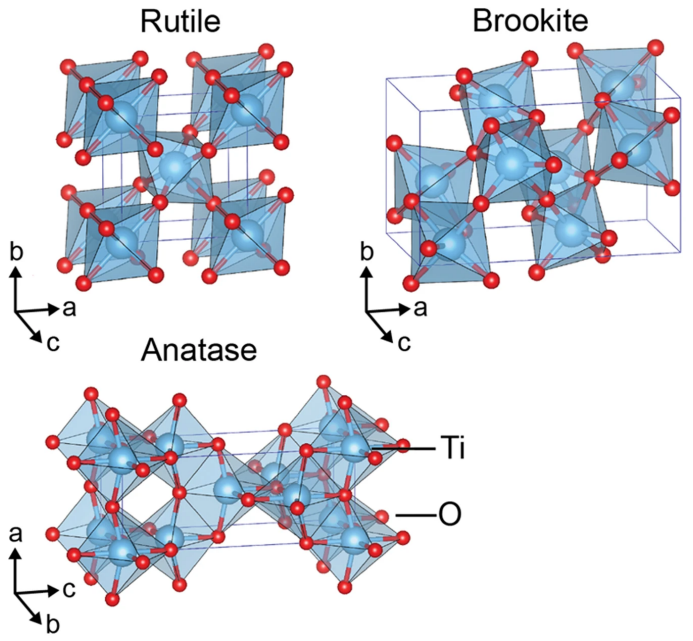

Figure 2.2: Crystal structures of TiO2 rutile, brookite and anatase polymorphs. [17]

those of graphite [19]. It should however also be possible to fabricate a Magnéli type compound directly, without the intermediate step of reducing TiO_2 [19].

Raman spectroscopy can be used to measure changes in lattice structures, and should therefore be able to reveal the presence of Magnéli phases in our samples. These are however very specific structures that we do not expect to encounter in our samples. Additionally, it is found that a stable charge ordered state exists only for Ti_4O_7 [18].

2.4.3 Chromium nitride (CrN) and chromium(III) oxide (Cr_2O_3)

Other materials that will be relevant in this present work are CrN and Cr_2O_3, with mineral names *carlsbergite* and *eskolaite* respectively. As the intent was to co-dope TiO_2 with equal amounts Cr and N, a CrN target was used to deposit the co-dopant. For reference, films were deposited only using the CrN target, one with N_2 background gas and one with O_2, as will be explained further in section 4.1. CrN thus is a relevant material, while Cr_2O_3 became relevant after earlier measurements made with variable angle spectroscopic ellipsometry (VASE) revealed Cr_2O_3 content in the film grown from CrN deposited with O_2 background gas. Somehow, this film was oxidised, though it is not known whether the film was deposited as CrN and then oxidised or if the Cr atoms oxides in the plasma plume during deposition or right after deposition onto the substrate. These materials will however not be studied in detail, as it is their incorporation into TiO_2 as dopants that is the focus of this work. Their Raman spectra will however be of relevance for analysing the obtained Raman spectra, presented in chapter 5.

It should be mentioned that chromium nitride, including the cubic CrN structure, also can form the hexagonal Cr_2N [20], with the mineral name *oreillyite* [21].

2.4.4 Doped TiO_2 for electro-optical applications

Let us now asses how the previously mentioned properties of TiO_2 might be altered by doping the material, specifically how doping can affect the material's crystallinity and optical properties.

The band gaps of the anatase and rutile phases of TiO_2 are 3.2 eV and 3 eV respectively, and accordingly they show insulating behavior [16]. However, by creating oxygen vacancies, its conductivity can be increased. These vacancies are often created when TiO_2 is doped with transition metals. Doping might also affect the crystal phase of TiO_2, and it has been predicted that a room-temperature conversion of anatase to rutile can occur when doped with Co or Ni [22].

As earlier mentioned, what we are interested in is so-called co-doping of TiO_2, specifically for optical applications. Here, the intention is not only to increase conductivity, but create intermediate bands located withing the total band gap of the material. A reduction of the band gap is thus not the main goal, though as the band gap of TiO_2 is already to large for optical applications, a reduction of its band gap as a by-product of the co-doping would not impose a problem either. Theoretical studies indicate that several transition metals, when used as a co-dopant alongside N, can shift the absorption edges of TiO_2 to the visible-light region [9]. This energy band reduction is both due to the reduced conduction band minimum (CBM) and the formation of impurity energy levels (IELs) in the band gap [9]. Specifically, co-doping TiO_2 with Cr-N has been shown to be able to reduce the band gap with up to 1 eV [10]. For IBSCs, a reduction in the band gap is neither the main goal nor a significant problem. It bears however mentioning that it is important that the co-doping does not lead to a continuum of states all the way from the conduction band to a possible intermediate band. This will result in a solar that functions with a reduced single band gap, and not an intermediate band. These findings thus illustrate the potential use of co-doped oxide semiconductors in a variety of photovoltaic and photocatalytic applications, as the co-doping enables the oxide semiconductors to absorb light in the visible light range.

TiO_2 co-doped with Cr-N as a potential IB material was motivation behind the production of the samples studied during this master project.

3 Experimental methods

The aim of this chapter is to give an overview of the experimental methods used for the fabrication and characterization of the present samples, as well as their working principles. The methods and techniques in question are **pulsed laser deposition** (**PLD**) and **Raman Spectroscopy**.

3.1 Conventional and combinatorial PLD

The following section was provided for the author's preceding specialization project by Hogne Lysne and Turid Reenaas, and was included here for completeness [1]:

Pulsed laser deposition (PLD) is a thin film deposition technique. A target material placed in a vacuum chamber is ablated by a high intensity laser pulse and a plume of ablated material is formed, as illustrated in Fig. 3.1. The plume consists of highly energetic atoms and molecules that can be charge neutral or ionized. Material from the plume is deposited on to a substrate as illustrated to the right in Fig. 3.1. This process is repeated many times to build up a thin film, layer by layer. The ablated material is distributed non-uniformly in the plume into the vacuum chamber and onto the sample. Normally the substrate is rotated at a constant speed to give a more uniform thin film.

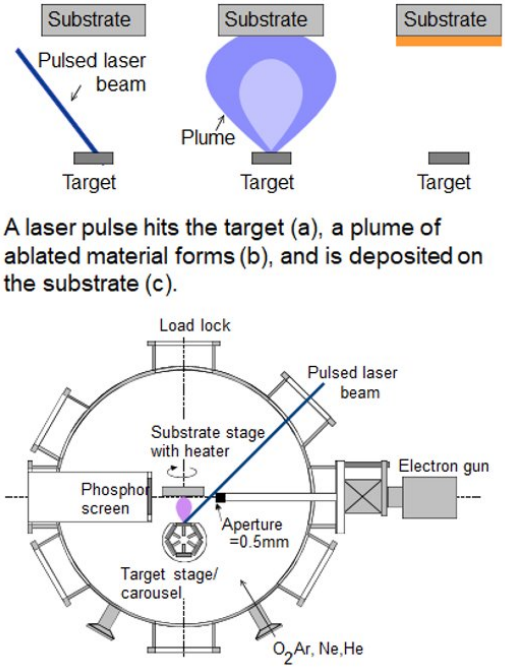

Figure 3.1: Top: schematic illustration of the PLD process. Left: A pulsed laser beam hits the target material. Middle: a plume of ablated material forms. Right: the ablated material deposits on the substrate to form a thin film. Bottom: Drawing of a typical PLD vacuum chamber. Notice how the laser enters from the top right, hits the target on the target carousel and forms a plume that hits the substrate. Also drawn in is an electron gun and phosphorus screen used on some PLD setups to perform in situ characterisation of the film growth.

Combinatorial PLD is a more advanced type of PLD where the non-uniformity of the plume is exploited to obtain a specific concentration and/or thickness gradient across the thin film. Multiple targets are used in combination to form plumes of different (combinations of) elements. The different plumes are deposited at specific positions on the substrate, and the thickness variation of the deposited material from each target/plume gives rise to concentration gradients in the thin film.

In the following a two target approach is described, but the concept can be extended to more target materials as well. First a few pulses of the first material is ablated and deposited while the substrate is kept stationary. Then the substrate is moved, for instance by a 180 degrees rotation, and a second target material is deposited by ablating a second target. This deposits more material straight across from the laser spot and less further away, to the sides. This is illustrated in Fig. 3.2 as a wedge for each of the materials. Each layer, consisting of two wedges, can be only a few atomic layers thick (typically less than 1 nm), depending on how much material is deposited in each step. The process is repeated many times to build up a film with a concentration gradient parallel with the substrate surface/across the substrate. In order to get a reasonable flat film for low doping concentrations, less material from target 1 (the dopant material) can be compensated for by ablating target 2 (the matrix material) at target 1 plume position on the substrate.

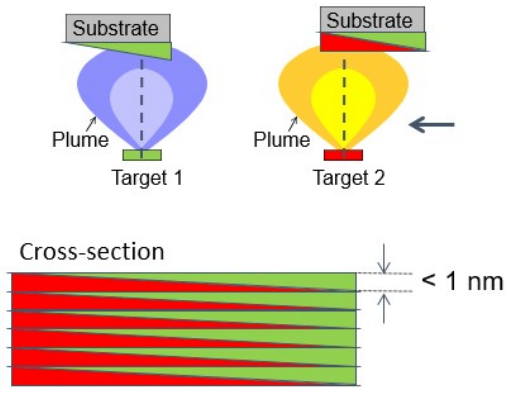

Figure 3.2: Schematic illustration of combinatorial PLD thin film growth. Top left: the first target material is ablated with a few laser pulses to give a thin film layer that is thick on one side of the substrate and thin on the other. Top right: The second target material is ablated after the substrate is moved. Bottom: by repeating the process a film with a concentration gradient is built up layer by layer.

3.2 Raman spectroscopy

Raman Spectroscopy is an analytical method used for chemical and structural analysis of a given material. It is based on the concept of *Raman Scattering* or the *Raman effect*, as explained in section 2.3. Raman spectroscopy usually utilises the Stokes Raman scattering. Anti-Stokes Raman scattering can also be used in Raman spectroscopy, but is usually not preferred, as it is less intense than the Stokes. It does however represent equivalent vibrational information of the molecule [15].

Though the name "Raman spectroscopy" typically refers to vibrational Raman using laser wavelengths which are not absorbed by the sample and thus scattered, there are many other variations of Raman spectroscopy that will not be mentioned in this thesis as they are beyond its scope. The specific equipment used during the present master project was a Raman spectrometer integrated with an optical microscope objective (from 5× to 100×) that focuses the laser beam onto the sample surface, so that the diameter of the laser spot on the surface of the sample typically is in the order of a few micrometers, often referred to as *micro-Raman spectroscopy*, though this term usually is associated with the integration of image mapping of the obtained Raman data. Focusing the laser beam makes it possible to conduct measurements over smaller areas at a time, and measure variations over smaller distances on a given sample. Similarly, techniques like *tip-enhanced Raman spectroscopy* can conduct measurements with nanometre-scale spatial resolution [23]. These techniques are however, as mentioned, beyond the scope of this thesis, as micro-Raman spectroscopy was the only technique utilized during this present master project.

As explained in section 2.3, by measuring the shift of the Raman scattered light, one can identify the different vibrational modes of the materials. As the shift is caused by vibrational modes characteristic of the species present in the sample as well as their structure, Raman spectroscopy can discover the chemical composition of materials and even distinguish between different crystalline phases of polymorphs. To quantify the shift of the scattered light, a monochromatic light source, such as a laser, has to be used.

There are however several challenges that need to be managed to before one can successfully characterise a sample using Raman spectroscopy. The main issue is arguably that Raman is a weak effect, far too weak to observe with the naked eye. Additionally, it is competing with stronger effects that can mask Raman information, the main opponent being *photoluminescence* (PL). PL comprises both *fluorescence* and *phosphorescence* processes and originates from an absorption/emission process between different electronic energy levels in the material [15]. Thus, PL is typically much stronger in intensity than Raman scattering, and can provide an unwanted broad background that can mask the Raman bands. Raman spectrometers are equipped with multiple features to combat these issues, and these systems usually consist of [15]:

- one or more monochromatic light sources (normally lasers)
- for micro-Raman spectroscopy, lenses (both to focus the light onto the sample and to collect the scattered light)
- filters (to purify the reflected and scattered light so that only the Raman light is collected)
- a means of splitting the light into component wavelengths, i.e. a spectrum (normally a diffraction grating or prism)
- a highly sensitive detector (to detect the weak light)
- a device such as a computer to control the whole system, display the spectrum and enable this information to be analysed

Still, some materials can prove difficult to characterise using Raman spectroscopy. As mentioned earlier, pure metals do not Raman scatter, as they reflect the light [15]. Amorphous materials are also challenging to characterise using Raman spectroscopy. Even though they do Raman scatter, they tend to produce broad and undefined spectra that are difficult analyse. The reason for this is that there is neither a real nor reciprocal lattice in an amorphous solid, and because of the absence of long-range translational symmetry and a corresponding reciprocal lattice, one detects scattering from local vibrational modes. Thus, the Raman spectrum of an amorphous solid resembles the phonon density of states for the equivalent crystalline form of the material, and very broad bands appear in their first order Raman spectra [24].

3.2.1 What information is obtained from a Raman spectrum

The Raman spectrum of a material can provide a lot of information about its structure and composition. You can study changes in the details of the spectrum, such as the height, width, and position of the Raman bands, and determine things like the relative amount of material, layer thickness (from monolayer up to hundreds of nanometers), crystallinity, whether it is under compression or tension and temperature [15].

Figure 3.3 shows an example of two different Raman spectra obtained from two different materials [15].

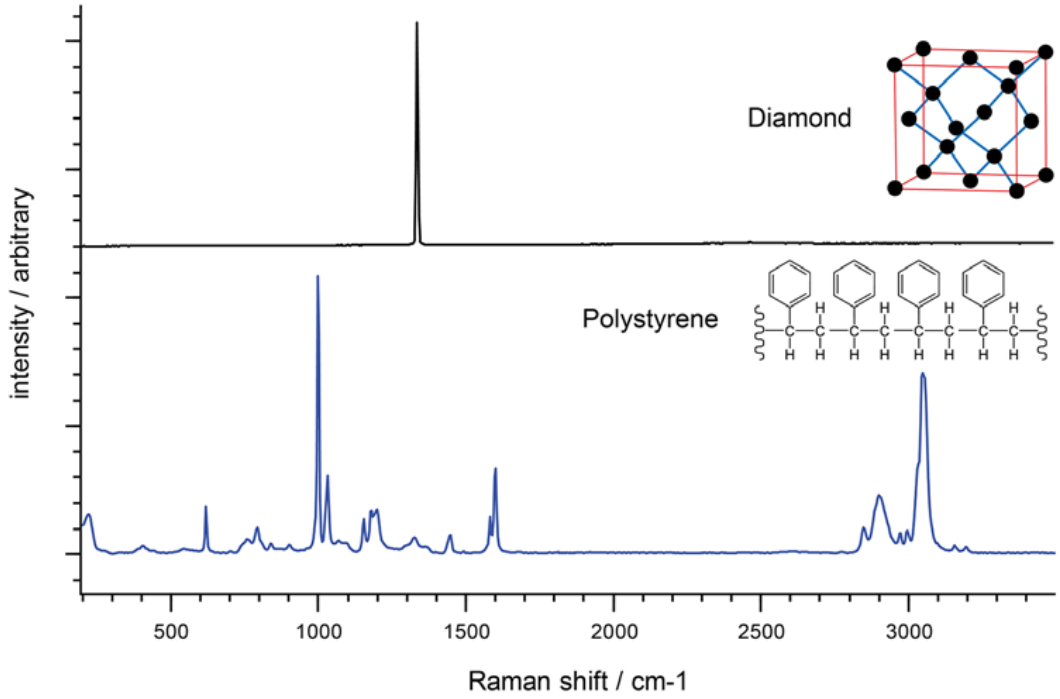

Figure 3.3: Raman spectra of diamond and polystyrene. [15]

These spectra illustrate the contrast between the Raman spectrum of crystals with a regular array of identical atoms all in the same configuration (such as the carbon atoms in *diamond*), and more complex compounds. In the cases of these crystals, you often see just one dominant Raman band (because there is just one molecular

environment of the crystal). In contrast, the Raman spectrum of *polystyrene* is much more complex because the molecule is less symmetric and has hydrogen atoms in addition to carbon atoms. There are also different bond types connecting the atoms, which will give rise to different vibrational modes and in turn different Raman shifts.

As mentioned, the position of the peaks in a Raman spectrum, i.e. the characteristic Raman frequencies of the sample, will correspond to the different vibrational modes of the material, providing a fingerprint that corresponds to the chemical composition and structure of a material. The variation in intensity of these Raman peaks can tell us the crystallographic orientation of the sample, and variation in absolute/relative intensity indicates the absolute/relative concentration of its corresponding species. Variations in Raman band width can correspond to both variations in crystallinity, but also variations in temperature. It is therefore preferred to keep one of these constant. Lastly, variations in Raman band position can be attributed to different stress states of the crystal [15].

While Raman data often are mainly analysed more qualitatively, more quantitative analysis methods can also be applied [25, 26].

4 Experimental setup/details and data analysis

The aim of this chapter is to give an overview of and explain the details and setup of the experimental methods used for fabrication and characterization of the samples.

4.1 Thin film/sample simulation and thin film growth

The following section was also provided for the author's preceding specialization project [1] *by Hogne Lysne and Turid Reenaas, and was reworked for this master thesis. The aim of this section is to explain the deposition simulation and fabrication of the samples that were studied both during the author's preceding specialization project and present master work. Note that the "project" that this section refers to is the PhD project of Hogne Lysne and Thomas Vågenes Brakstad.*

A goal of this project is to establish combinatorial PLD thin film growth as a technique in the research group. This is accomplished by an iterative process of optimization by simulations and feedback from actual thin film growth.

The simulations were performed in an in house developed code library called pyPLD. This code simulates PLD deposition by modeling the material deposition from one single laser pulse and then adding this to the substrate for each laser pulse of the deposition. This is done while keeping track of the substrate movement, either constant rotation for conventional PLD or movement in between materials in combinatorial PLD. For the setup used in this work the movement between materials in combinatorial PLD were performed by a 180 degrees rotation while keeping the laser spot position away from the substrate rotation axis.

To be able to simulate the deposition of the combinatorial films we need to have a mathematical model of the amount of material deposited on the substrate for each laser pulse/each plume. To establish this we deposited a high number of pulses without moving the substrate for each target material. The thickness of the resulting film (called "plume sample") is mapped by variable angle spectroscopic ellipsometry (VASE). The thicknesses obtained from VASE are divided by the number of pulses and fitted to a theoretical model for the material distribution from a single laser pulse. This theoretical model for the material deposited for each plume/pulse is used as input to the simulations of the PLD thin films.

For the growth of Cr,N-doped TiO_2, we used a TiO_2-target and a CrN-target. The simplest case would be if we could grow the complete film with the same process gas (oxygen) during the growth. However, initial studies revealed that the ablated CrN would form Cr_2O_3 if the PLD chamber was filled with O_2, while chromium nitride formed when the chamber was filled with N_2. We thus decided to ablate the CrN-target using N_2 background/process gas, and also to ablate a few pulses of TiO_2 while keeping the N_2 process gas in the chamber, to prevent the deposited Cr,N-doping from oxidizing into chromium oxide: We "*capped*" the Cr,N-doping with a few pulses of TiO_2 deposited with N_2 gas in the chamber. Then the process gas was changed form N_2 to O_2 for the deposition of the rest of the TiO_2. For the

simulations of the resulting combinatorial Cr,N-doped TiO_2 films, we thus deposited plume samples of the CrN-plume using both O_2 and N_2 as process gas, in addition to a plume sample of the TiO_2 using O_2, and TiO_2 using a cycling of N_2 and O_2.

Based on the mathematical models of the various plumes, the growth of a combinatorial thin film was simulated and the simulation was used as input to the actual growth of the combinatorial films. This was a TiO_2 film doped with Cr and N from a CrN target. As described above, a capping scheme was established to try to ensure incorporation of N into the thin film, where the background gas was alternated between N_2 and O_2. In addition a reference film was deposited in exactly the same manner as the combinatorial film, but omitting the CrN pulses. The pulses were replaced with a 9 s wait to maintain the same thermal history and gas cycling for the films. This process is shown in algorithm 1, and explained below. Please note that TiO_2 and CrN was deposited with the laser repetition frequencies 5 and 10 Hz respectively.

- For the combinatorial thin film, the background gas was changed repeatedly between a constant O_2 flow and a constant N_2 flow during the deposition. The CrN was deposited under N_2 flow, while (most of the) the TiO_2 was deposited under av O_2 flow. The laser spot was positioned at 13 mm from the substrate centre. At 0 deg rotation, 26 TiO_2 pulses were deposited under O_2 flow. At 180 deg rotation, the gas was changed to N_2, followed by a 30 sec pause to let the gas flow settle, before 90 CrN pulses were deposited. Then 10 TiO_2 pulses were deposited, with the purpose of capping the CrN before the O_2 gas was let into the chamber again, after a new 20 sec pause. Next, the gas was changed back to O_2, the gas flow was settled again during a 30 sec pause, and finally 12 TiO_2 pulses were deposited.
- The combinatorial reference film was deposited in exactly the same way as the combinatorial film above, except that the CrN pulses were replaced with a 9 s wait.

Simulations were also done to optimize conventional PLD of TiO_2 thin films (with a continuously rotating substrate), to obtain films as flat as possible (within the desired region of the substrate). The optimization with respect to film flatness was performed by simulating thin films deposited for different substrate positions, and finding positions resulting in films with the lowest variation in thickness within the area of interest on the substrate. Thin films with rotating substrate were deposited both with regular and optimized positions.

In table 4.1 and 4.2 an overview of all the deposited "plume", "film" and "combinatorial samples" are given, as well as their respective deposition parameters. The shift is the position of the deposition in x- and y-direction, relative to the centre of the substrate. The sample names represent their respective sample category, and the parameters that separate the different samples of same category. The name of "plume samples" start with a P for "plume", and following are a summary of their respective deposition parameters, namely target (T = TiO_2, C = CrN), background gas (O_2, N_2 or cycling between both), and substrate temperature. The two "film

samples", starting with F, are only separated by the shift in their deposition position. Thus this is the only parameter given in the name. The "combinatorial samples" have names starting with CF (for "combinatorial film"), and are then separated by either being doped with the CrN target (CFCrN), or being the reference sample (CFRef).

Algorithm 1 Combinatorial film deposition with capping; one with CrN-doping (COMB) and one reference sample (REF) without doping.

$Gas\_flow \leftarrow 1.3 \times 10^{-2}\,\mathrm{torr}O_2$
for 400 loops **do**
  $Substrate\_rotation \leftarrow 0°$
  $Deposit \leftarrow 26\_pulses\_TiO_2@5Hz$
  $Substrate\_rotation \leftarrow 180°$
  $Gas\_flow \leftarrow 1.6 \times 10^{-2}\,\mathrm{torr}N_2$
  $Wait \leftarrow 30\,\mathrm{sec}$
  if COMB sample **then**
    $Deposit \leftarrow 90\_pulses\_CrN@10Hz$
  else if REF sample **then**
    $Wait \leftarrow 9\,\mathrm{sec}$
  end if
  $Deposit \leftarrow 10\_pulses\_TiO_2@5Hz$
  $Wait \leftarrow 20\,\mathrm{sec}$
  $Gas\_flow \leftarrow 1.3 \times 10^{-2}\,\mathrm{torr}O_2$
  $Wait \leftarrow 30\,\mathrm{sec}$
  $Deposit \leftarrow 12\_pulses\_TiO_2@5Hz$
end for

Table 4.1: Overview of deposited plumes and (flat) films. The 5 plume samples/films are those deposited with no rotation.

Sample	Target	Pulses	Rotation speed	Back fill gas		Temperature	Shift [x,y]
			[deg/sec]	O_2 [torr]	N_2 [torr]	[°C]	[cm]
PTO700	TiO_2	15 000	0	1.3×10^{-2}	0	700	[0.33,1.63]
PTO550	TiO_2	5 000	0	1.3×10^{-2}	0	550	[0.33,1.63]
PTON550	TiO_2	5 000	0	1.3×10^{-2} [a]	1.6×10^{-2}	550	[0.33,1.63]
PCO700	CrN	40 000	0	1.3×10^{-2}	0	700	[0.33,1.63]
PCN550	CrN	40 000	0	0	1.6×10^{-2}	550	[0.33,1.63]
F0.33,1.63	TiO_2	18 000	29	1.3×10^{-2}	0	700	[0.33,1.63]
F0.0,3.0	TiO_2	36 000	29	1.3×10^{-3}	0	700	[0,3]

[a] For every 10 pulses deposited the background gas was cycled from N2 to O2 and held for 50 s before cycling back to N2.

Table 4.2: Overview of deposited combinatorial films.

Sample	Pulses @ position				Shift [x,y]
	1.3×10^{-2} torr O_2		1.6×10^{-2} torr N_2		
	TiO_2 @ 0 deg	TiO_2 @ 180 deg	TiO_2 @ 180 deg	CrN @ 180 deg	[cm]
CFRef	10400	4800	4000	wait 9 s [b]	[0,1.3]
CFCrN	10400	4800	4000	36000	[0,1.3]

[b] A wait of 9 seconds per loop replaces the time used for the 90 pulses from the CrN target in the combinatorial sample.

4.2 Sample characterization using Raman spectroscopy

Raman spectroscopy was used to characterise the structural and crystalline composition of the thin film samples. The chemical composition of the samples were for the most part known beforehand. The Raman setup used was a *Renishaw InVia Reflex Spectrometer System for Raman spectral analysis* using VIS excitation laser at 532 nm (100mW), with 2400 l/mm grating and 100x objective lens, with a spectral resolution less than 1 cm^{-1}. The exact laser spot diameter is not known, but from the specifications of the equipment, and comparing to other research that have used the same equipment [26, 27], the laser spot diameter is believed to be less than 1 µm.

The program included with the system, WiRE™4, was used to conduct the measurements and data acquisition, as well as to analyse the obtained data. Though the equipment was capable of advanced micro-Raman mapping techniques, only the *Spectral acquisition* measurement setup was used, more similar to a traditional Raman spectroscopy, but with a micro-Raman laser spot. The scan types available were *Static* and *Extended*. *Static* is a quicker scan that covers a limited range on either side of a chosen spectrum range centre. This range depends on the wavelength and the grating used, and varies from about 200 to 500 cm^{-1} on either side of the range centre. *Extended* scans between an entered upper and lower limit using SynchroScan™, Renishaw's patented method of acquiring wide-range spectra, with full range extended scan at high spectral resolution $>$ 100-4500 cm^{-1} for VIS lasers.

With the wavelength and grating used for this project, and because the samples were inorganic and mostly crystalline, the *static* scan range was large enough to cover the entire spectrum. *Extended* scans was then used to perform measurements in the specific ranges between the most intense peaks while increasing the laser intensity to study the details of the spectrum without oversaturating the detector. In that respect, the term *extended* scan might be somewhat misleading when used here, and purely refer to the term used by the system software. Still, the author chose to refer to these system terms for reproducibility of the presented results.

The obtained data was then analysed using WiRE™4 and plotted with Python, using the Matplotlib library.

4.2.1 Raman spectra in literature and databases, for reference

To better conduct the experiments, Raman spectra of materials similar to the ones that should be present in our samples were searched for in literature and works of reference. In this section, literature and references will be presented to give an overview of the spectra expected from the relevant materials.

In addition to references from literature, reference data from The RRUFF™Project [28] will be presented. The RRUFF™ Project [28] is a website containing a database of Raman spectra, X-ray diffraction, and chemistry data for minerals, and provides reference spectra of numerous minerals as ASCII files [26]. The RRUFF™ database [28], was used to gain insight into what Raman peaks can be expected from the relevant materials. Data from database was also acquired with a laser of wavelength 532 nm.

Also "processed" data was chosen in stead of the also available "raw" data. The raw files contain the spectra as measured, whereas the processed files contain the first-order scattering modes only.

Most of these database materials are bulk minerals, some of which were synthetically made. Thus, the data from this database is not directly comparable with the data obtained during this present project, but provide reference as the crystal phases should still mainly be found at or near the same Raman shifts. Also, as this is borrowed data, it has not been analysed in detail, but plotted as is with the peaks annotated at their max value, meant only as initial reference.

Si references

Figure 4.1 show the Raman spectrum of Si, acquired from the RRUFF™ database [28]. It mainly shows that Si has one very intense peak around 520 cm^{-1}. From literature it can be verified that this peak can be attributed to Si [26, 29]. Additionally, one should expect to see a peak from Si around 300 cm^{-1} and a wider band between 900 and 1050 cm^{-1} [26, 29]. These are however less intense, and are only barely noticeable in figure 4.1.

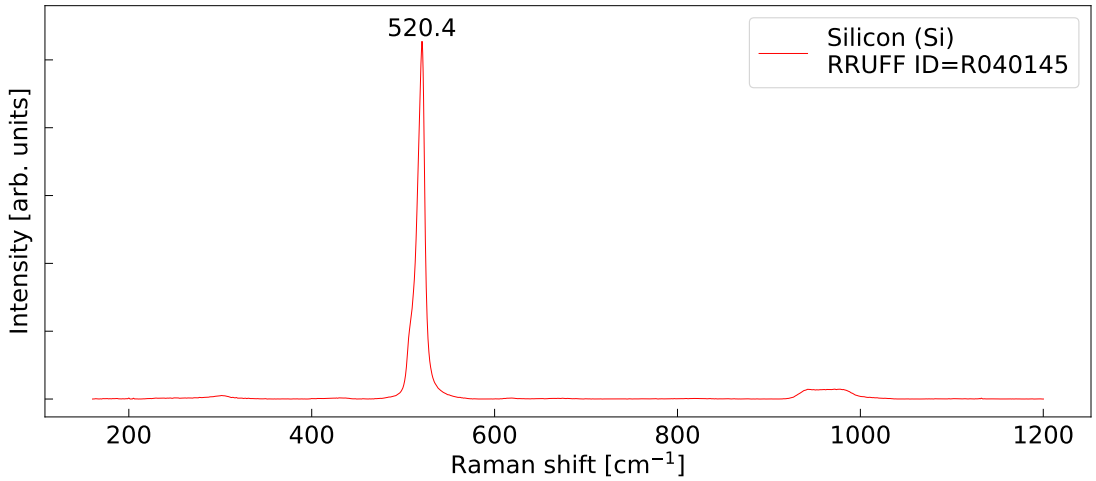

Figure 4.1: Raman spectrum of Si, acquired from [28].

TiO_2 references

Figures 4.2 and 4.3 show show the Raman spectra of anatase and rutile respectively, acquired from the RRUFF™ database [28]. Brookite is, as previously mentioned, highly unstable compared to anatase and rutile [16]. Thus, we do not expect to observe it in our samples, and the spectrum of brookite will not be included here for the sake of brevity.

Figure 4.2 shows the dominant anatase peak at around 144 cm^{-1}, which corresponds to what is found in literature [26, 30, 31, 32]. The remaining, less intense anatase

peaks should then according to literature be found around 197, 399, 513, 519 and 640 cm^{-1} [30, 31, 32]. This mostly correspond to spectrum in figure 4.2, though with some shift present.

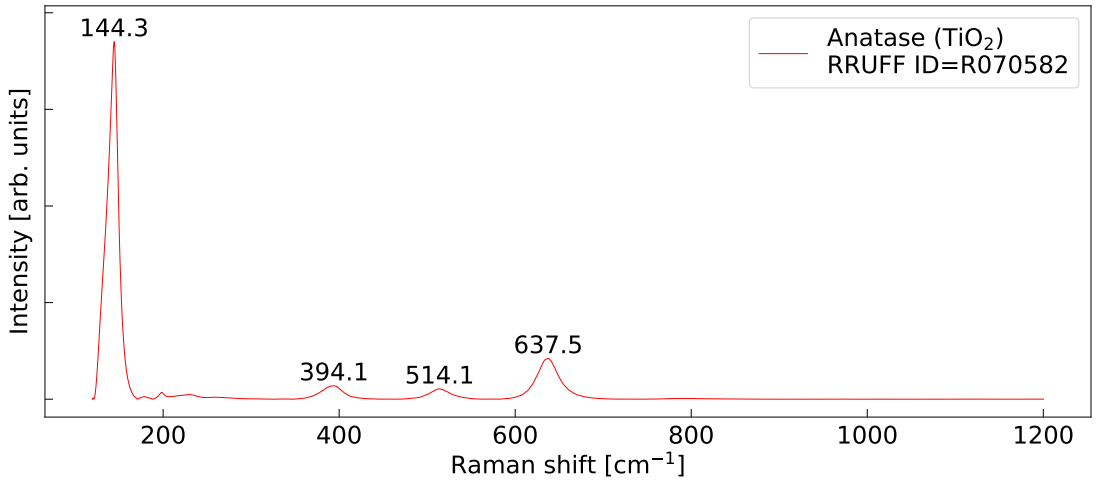

Figure 4.2: Raman spectrum of anatase, acquired from [28].

As our thin films are deposited on Si, the weaker anatase peaks around 513, 519 cm^{-1} likely will coincide with the strong Si peak around 520 cm^{-1}, and are thus less useful.

Figure 4.3 shows the spectrum of rutile. According to literature, its dominant peak should be around 612 cm^{-1} [26, 30, 31]. It should also have less intense peaks around 143, 447 and 826 cm^{-1} [30, 31], as well as around 240 cm^{-1} [19]. This somewhat corresponds to figure 4.3.

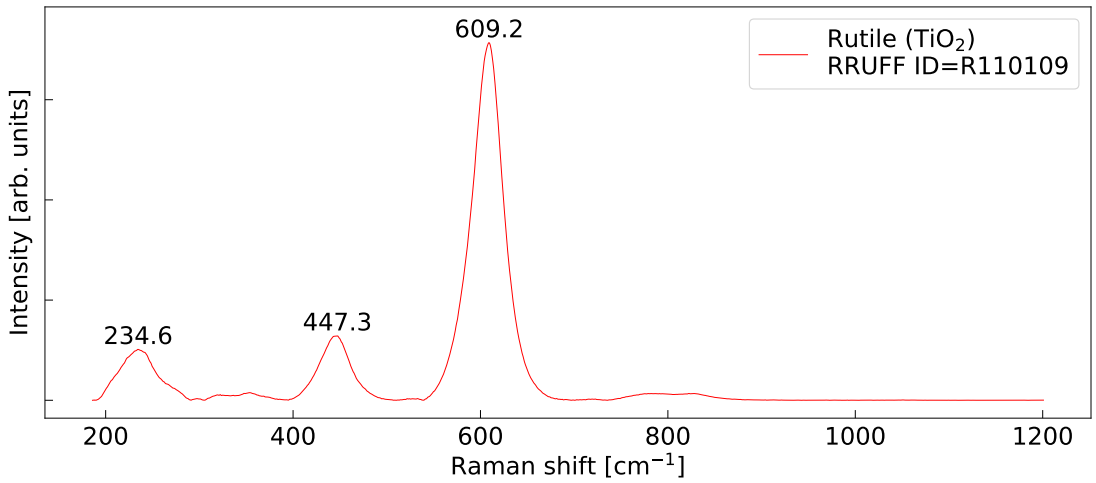

Figure 4.3: Raman spectrum of rutile, acquired from [28].

References for CrN and Cr_2O_3

The RRUFF™ database [28] had no record of CrN (carlsbergite). According to literature, it should however have a Raman spectrum with peaks at 238 and 619 cm^{-1} [33], though it appears that CrN thin films possess a strain/stress which results in poorer than theoretically expected performance [34], and thus might be of poor crystallinity. Starting with pure Cr, as nitrogen is added, initially N atoms occupy interstitial positions in body-centered cubic Cr and when the amount of N increases an amorphous structure emerge [34].

Figure 4.4 show the Raman spectrum of Cr_2O_3 (eskolaite), acquired from the RRUFF™ database [28]. It was found in literature that its dominant peak should be around 551 cm^{-1} [27, 35], with weaker peaks around 296, 350, 525 and 612 cm^{-1} [27]. Considering that this article only measured the spectrum between 200 and 675 cm^{-1}, this mostly corresponds to the spectrum in figure 4.4, though it does not fully account for the peaks around 654 and 688 cm^{-1}.

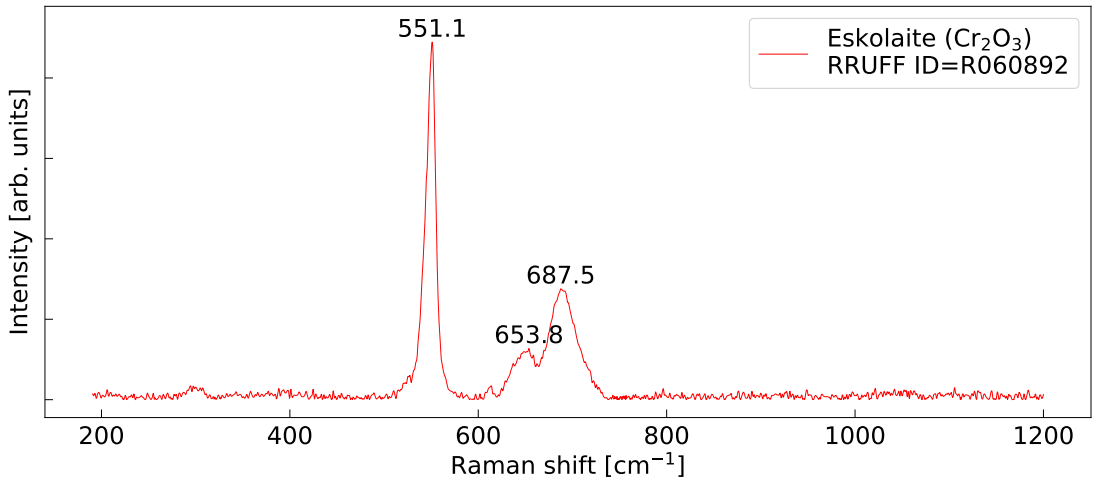

Figure 4.4: Raman spectrum of eskolaite, acquired from [28].

References for doped TiO_2

It was also of interest to search through literature to see how doping might affect the Raman spectra of TiO_2. For Cr-doped anatase TiO_2, a red shift and broadening of the major peak was found, suggesting the incorporation of Cr ions into the TiO_2 lattice which is attributed to the increased disorder and destruction of ideal symmetry of the crystal [36]. In this article it can be seen that with an increase in the Cr concentration, there are no phases corresponding to Cr or related oxides, suggesting that all the Cr atoms have been substituted into the lattice rather than occupying the interstitial sites associated with Ti [36]. This research was however studying Cr-doped TiO_2 nanocrystals derived by a sol–gel method, so not fully comparable to our thin film samples.

Research on TiO_2-Cr_2O_3 was also studied. In one article, the peak positions of

the dominant Cr_2O_3 and rutile TiO_2 modes are found to be red shifted from their characteristic peak positions; but no shift is detected due to the intermixing of Cr_2O_3 and TiO_2 phases [35].

Another article showed TiO_2-Cr_2O_3 nanolaminates grown on different substrates by atomic layer deposition [37]. Here, the crystalline phase of TiO_2 was rutile in the laminate grown on sapphire (Al_2O_3) and anatase in the laminate grown on Si and SiO_2. All laminate also contained Cr_2O_3. No shift was observed when TiO_2 was in the anatase phase, but a shift in the dominant Cr_2O_3 peak was observed when TiO_2 was in the rutile phase, from 550 to 557 cm^{-1}. The shift is attributed to the in-plane compressive strain in Cr_2O_3 [37].

4.2.2 Scanning parameters and experimental procedure

Based on the knowledge acquired from the above mentioned literature and database references, the following measurement procedure was established:

1. **Survey scan** - Static scan with range centre 650 cm^{-1} and laser intensity at 10 % for 1 second. Quick scan of the entire spectrum, mainly to identify the Rayleigh-peak at 0 cm^{-1} and the most intense Si-peak around 520 cm^{-1}, to monitor the calibration and stability of the equipment.

2. **Lower spectrum scan** - Extended scan in the range 70-450 cm^{-1} and laser intensity at 10 % for 10 seconds. Detailed scan in the lower spectrum range between the Rayleigh-peak at 0 cm^{-1} and strong Si-peak around 520 cm^{-1}. It should be noted that there still is a sharp Si-peak around 300 cm^{-1} with tails reaching from around 200-450 cm^{-1}.

3. **Upper spectrum scan** - Extended scan in the range 570-900 cm^{-1} and laser intensity at 10 % for 10 seconds. Detailed scan in the upper spectrum range between the strong Si-peak around 520 cm^{-1} and -band starting at around 900 cm^{-1}. As the relevant materials are all inorganic the range above this upper Si-band is of little interest, as can also be observed from figures 4.1-4.4.

As a standard, all measurements were also conducted with 3 accumulations. These measurements were conducted in each position of measurement on every sample. For some of the samples it was however necessary to alter these parameters to obtain the best possible results. This mainly consisted of increasing the laser intensity to 50 % during the detailed scans if the signal was weak or noisy. These alterations will be mentioned and explained for the relevant samples during the next chapter.

Sample placement and orientation

Figure 4.5 shows a wafer sample placed on microscope slides inside the chamber of the Raman equipment, to be subjected to measurements. All samples were placed similarly on the stage, with the wafer flat parallel to the left side of the slides and

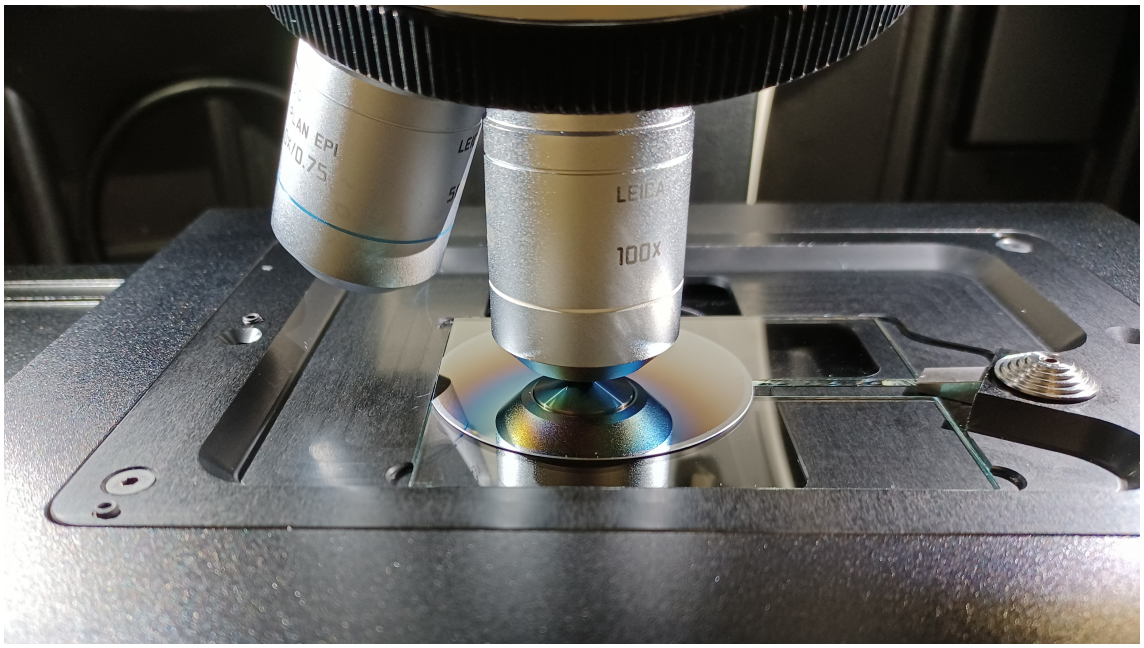

Figure 4.5: Photo of wafer with deposited thin film in standard placement on the stage inside the chamber of the Raman equipment, showing the elevation of the lens after focusing the laser. (The sample shown in this picture is PCO700.)

the wafer edge tangent parallel to the upper edge of the slides, as seen in figure 4.5. Note that this is "upside down" from how the samples will be oriented during the presenting of the results in the following chapter. The wafer samples were then oriented visually against their origo. From here the stage could be moved so that the measurements could be performed in the desired positions. For the samples with a visible "plume centre", the position of their "plume centre" would usually also be found or confirmed through visual analysis.

As all samples were placed in the same way, and comparing the origo positions that were found on different sessions, this method proved accurate within the needs of these experiments, and much faster and simpler than other methods of orientation that would involve using the image feed of the microscope lens etc. All samples are thus assumed to be well oriented, within an uncertainty of ± 1 mm. It should be mentioned that there is some uncertainty associated with the placement of the substrate in the wafer holder before deposition as well, both in position and rotation. In this thesis, this uncertainty will however be assumed to be insignificant, though it will add to the uncertainty of the sample orientation of the characterisation process.

5 Results and discussion

Like with the author's preceding specialization project [1] and as earlier mentioned in the previous chapter, the samples will be mainly categorised as either "*plume samples*", "*film samples*" or "*combinatorial samples*".

The results will be presented one sample at a time, and the results from each sample will be presented in a way that best illustrates what is interesting about the results of each sample. Thus, all samples will not be analysed with the same level of detail. The chapter will then end with a compilation and comparison of the related results and samples, and a proposition of possible improvements and future work.

The program WiRE™4, which was included with the Raman spectroscopy equipment, was used both to conduct the measurements and to analyse the obtained data. For most of the more unambiguous data, the "Peak pick" function of WiRE™4 was used to find the exact peak locations of the obtained spectra. In the cases where the obtained spectra contained overlapping and more ambiguous peaks that were harder to analyse qualitatively, WiRE™4 was used to add fitted curves, for more detailed analysis. The fitted curves are a mix between Gaussian and Lorentzian functions, and will be presented along with their respective parameters, including a % Gaussian providing the ratio between Gaussian and Lorentzian function, as well as the *chi-square* value from the test for goodness of fit to the corresponding spectrum. Chi-square is a quantity commonly used to test whether any given data are well described by some hypothesized function, and is the sum of the square of the ratio of the distance of a point from the curve divided by the predicted standard deviation at that value of x. Its mathematical definition beyond this will not be discussed further in this thesis. For presentation, the obtained and analysed data was plotted with Python, using the Matplotlib library.

The stability and calibration of the Raman equipment was monitored by observing the variation in the Rayleigh peak and dominant Si-peak, at 0 and 520 cm^{-1} respectively, in the survey scans of each sample. As only random variations in either of the peaks was observed throughout the measurements, the data is believed to be real, with an uncertainty of around ± 0.1 cm^{-1}.

5.1 Si substrate

Firstly, data acquired from an Si substrate without any deposited thin film will be presented and analysed. This will be used as a reference when analysing the following data from the measured thin films, to better distinguish between the actual signal from the measured thin film and background signal from the Si substrate.

All measurements were made in the centre of the Si wafer.

Survey scan

Figure 5.1 show the spectrum acquired from the survey scan conducted in the centre of the Si substrate as delivered, both linearly and logarithmic with a base of 10. Additionally, vertical lines are added at Raman shift = 0 and 520 cm^{-1} to mark the Rayleigh-peak and dominant Si-peak respectively. This dominant peak around 520 cm^{-1}, corresponds to what is found in literature [26, 29]. These lines will be added to every following survey scan plot, as they give information about the calibration and stability of the system, and variation in especially the Rayleigh-peak will give an idea of the general uncertainty of the measurements. Here, this reveals no apparent shift in either peaks, implying that the equipment was stable during this set of measurements.

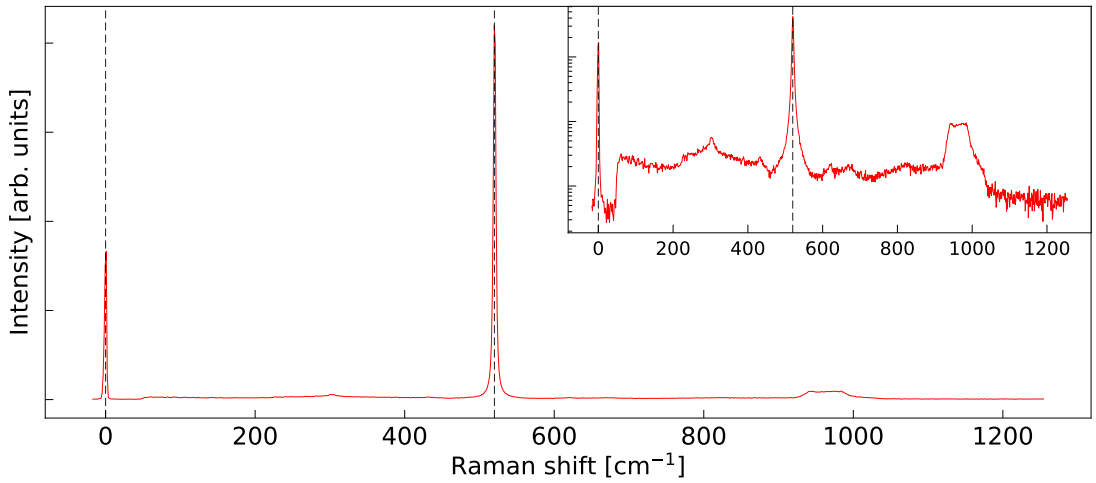

Figure 5.1: Raman spectrum of Si wafer as delivered. Vertical lines mark the Rayleigh-peak at 0 cm^{-1} and the most intense Si-peak 520 cm^{-1}.

Survey scans will be plotted like this as a standard, and thus the details of the plot will not be repeated for each sample as they will all be plotted equally. As the survey scans are mainly to monitor the calibration and stability of the system they will not be addressed thoroughly unless showing a clear deviation from what is expected or have already been observed and addressed in previous samples.

Lower spectrum scan

Figure 5.2 show the spectra acquired from the lower spectrum scan of the pure Si substrate, with annotations marking the peaks of the spectrum. A scan was made with both 10 % and 50 % intensity, to investigate the effect the laser intensity has on the shape of the spectrum. After normalising each spectrum against their respective largest peak, and plotting them on top of each other, it becomes apparent how the laser intensity does in fact affect the shape of the obtained Raman spectrum. This should be kept in mind when later comparing spectra obtained from scans at different intensities. As mentioned in the previous section, it will be mentioned explicitly when this is the case.

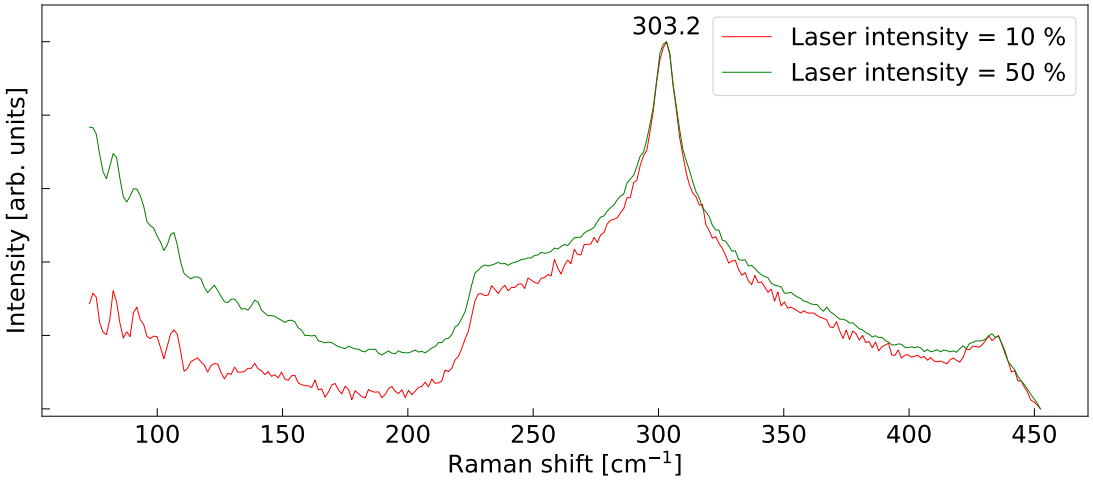

Figure 5.2: Raman spectra from lower spectrum scans of a pure Si-wafer, with laser intensities of 10 % and 50 %.

Both spectra show a peak around 303, which corresponds to what is found in literature [26, 29]. It should however be noted that this peak also has associated "tails" on each side.

Upper spectrum scan

Figure 5.3 show the spectra acquired from the upper spectrum scan of the pure Si substrate, again with annotations marking the peaks of the spectrum and scans made with both 10 % and 50 % intensity. The spectra were normalised against their respective largest peak and plotted on top of each other like in figure 5.2, still to show how the laser intensity affects the shape of the obtained Raman spectrum.

As the peaks are less intense in this part of the spectrum, the increase in laser intensity also shows a visible increase in signal-to-noise-ratio. This supports the choice of increasing the laser intensity where a lower laser intensity scan provides spectra with a weak and noisy signal.

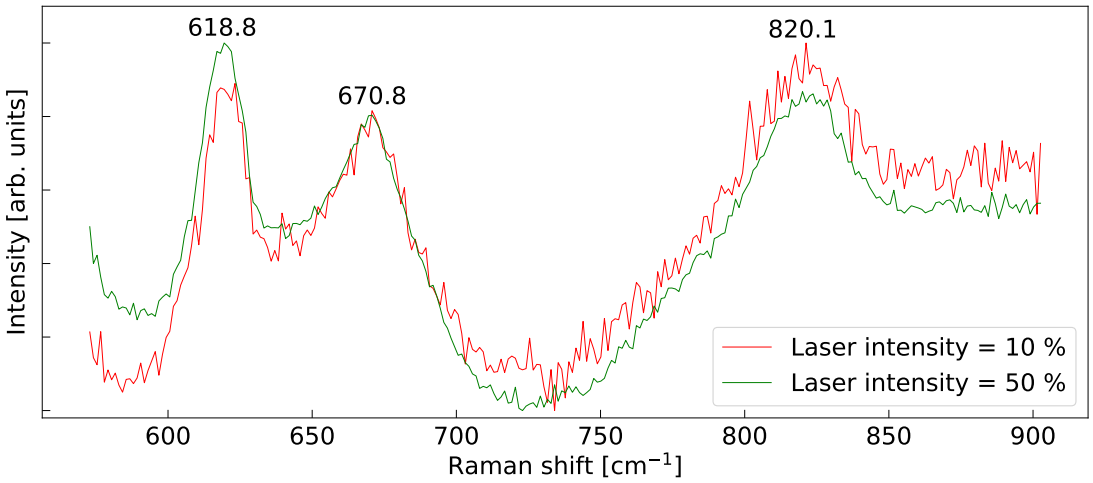

Figure 5.3: Raman spectra from upper spectrum scans of a pure Si-wafer, with laser intensities of 10 % and 50 %.

None of these peaks are accounted for in the cited literature [26, 29]. This is however a very detailed scan, and these are not typically sharp peaks. There is no reason to believe that the Si substrate should contain any significant contamination, and so this spectrum is contributed to crystalline Si.

5.2 PTO700

Firstly to be presented, are the results obtained from samples with films grown with the substrate staying stationary throughout the deposition, creating films with visible interference fringes corresponding with the shape of the deposition plume. These have therefore been named "*plume samples*". This initial sample, and the following two samples, were deposited with a TiO_2 target. The Raman spectra of this initial sample show clear signs of anatase.

The measurements were carried out in the the following three positions, given relative to the centre of the wafer, with the flat oriented to the right, as shown in figure 5.4:

- **Pos. 1**: (4202,15637) µm. 'Plume centre'.
- **Pos. 2**: (4202,-3182) µm. 'Midpoint'.
- **Pos. 3**: (4202,-22000) µm. 'Film edge'.

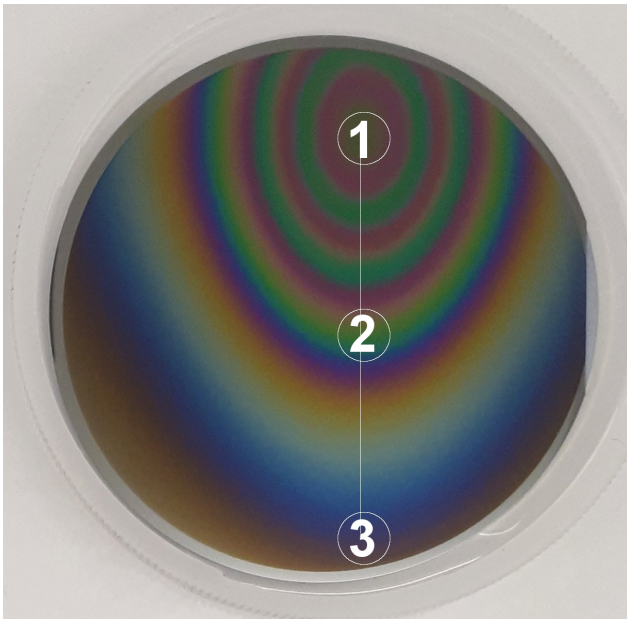

Figure 5.4: Photography of the wafer sample PTO700, and a schematic of the positions of measurement.

Survey scan

Figure 5.5 show the spectra acquired from the survey scan conducted in all positions of measurements on the present sample. This reveals no apparent shift in either the Rayleigh peak or dominant Si-peak, at 0 and 520 cm^{-1} respectively, in either of the positions, implying that the equipment was stable during this set of measurements. As this is expected to be the standard case for all measurements, this will not be commented on for the following samples, unless the system should appear unstable during the session of measurements or uncalibrated from the start of the session.

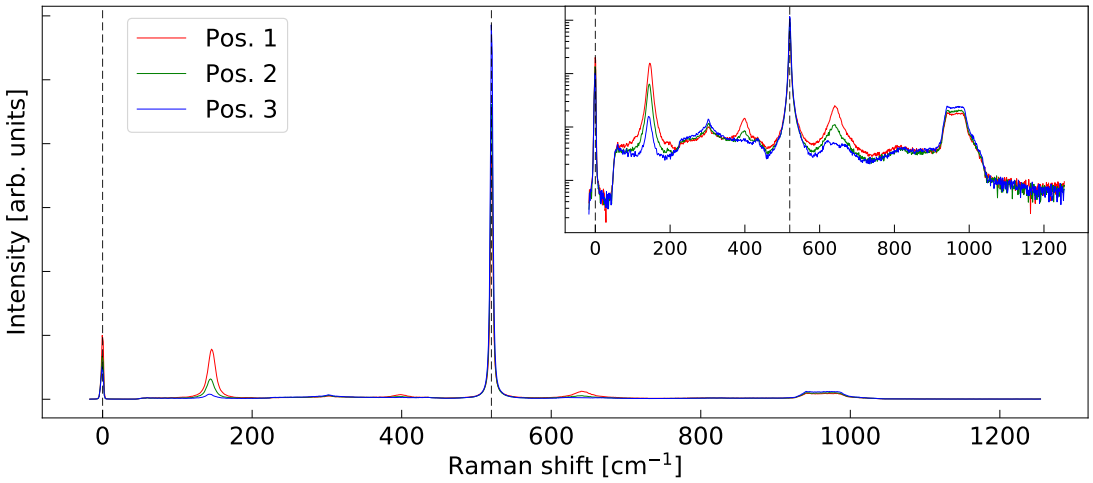

Figure 5.5: Raman spectra from survey scans in each position of measurements of the sample PTO700. Vertical lines mark the Rayleigh-peak at 0 cm^{-1} and the most intense Si-peak 520 cm^{-1}.

From the survey scan we can already observe the strong anatase peak at around 144 cm^{-1}, and that it's intensity decreases away from the "plume centre" and towards pos. 2 and 3. The intensity of the Si peak at around 520 cm^{-1} however increases away from the "plume centre". Both cases can be attributed to the fact that the film thickness decreases away from the "plume centre".

Lower spectrum scan

Figure 5.6 show the spectra acquired from the lower spectrum scan conducted in all positions of measurements on this sample, with annotations marking the peaks in each spectrum and each spectrum equally shifted in the y-direction relative to each other. Additional annotations mark which materials the peaks can be attributed to. The spectrum from the equivalent scan of the Si substrate has also been added for reference and normalised to match the corresponding Si peak in the pos. 3 spectrum. All measurements were made with standard parameters and 10 % laser intensity, including the Si substrate scan.

The first peak shown in this part of the spectrum belongs to anatase, and one can observe a small shift in peak value, likely caused by a difference in stress from the "plume centre" towards the wafer edge, though the peak in pos. 2 is closest to the reference value of 144 cm^{-1} found in literature [26, 30, 31, 32]. This peak is also noticeably more intense towards the "plume centre" corresponding to the thickness of the deposited film, and the differences in stress across the sample could arrive from the difference in film thickness [30]. Towards the end of this chapter, during section 5.11, the shift in this peak will be plotted and compared to the similar peak shift of other samples with spectra showing signs of anatase.

Also observable is the Si-peak at 303 cm^{-1} and the less intense anatase peak at around 398 cm^{-1}.

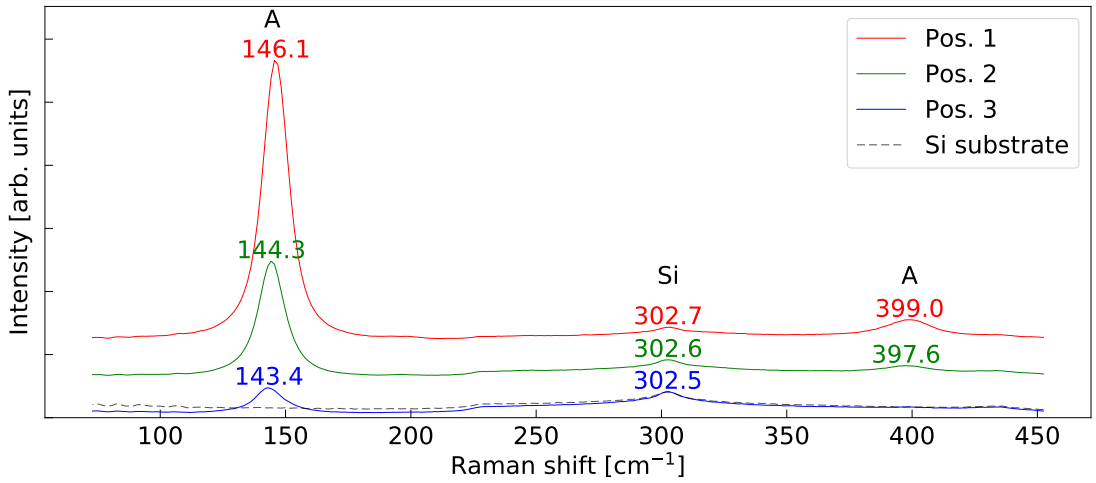

Figure 5.6: Raman spectra from lower spectrum scans in each positions of measurements of the sample PTO700, equally shifted in the y-direction relative to each other, as well as the equivalent scan of the Si substrate for reference. "A" marks anatase peaks, while "Si" marks the silicon peak.

Upper spectrum scan

Figure 5.7 show the spectra acquired from the upper spectrum scans. Here the scan in pos. 3 was conducted with a laser intensity of 50 %, for better signal-to-noise-ratio. To compensate for the differences in intensity between the scans made with 10 % and 50 % intensity, all spectra in figure 5.7 are normalised against their most intense peak. The spectra have then been plotted equally shifted in the y-direction relative to each other. Additional annotations mark which materials the peaks can be attributed to. The spectrum from the equivalent 50 % laser intensity scan of the Si substrate has also been added for reference, normalised against its most intense peak and shifted to match the lowest value of the scan from pos. 3.

The spectra in figure 5.7 show the other peak from anatase, with a reference value at around 640 cm^{-1} [30, 31, 32]. This peak also shows a shift between the positions. The rest of the peaks are attributed to Si, by comparison to the spectrum from the Si substrate.

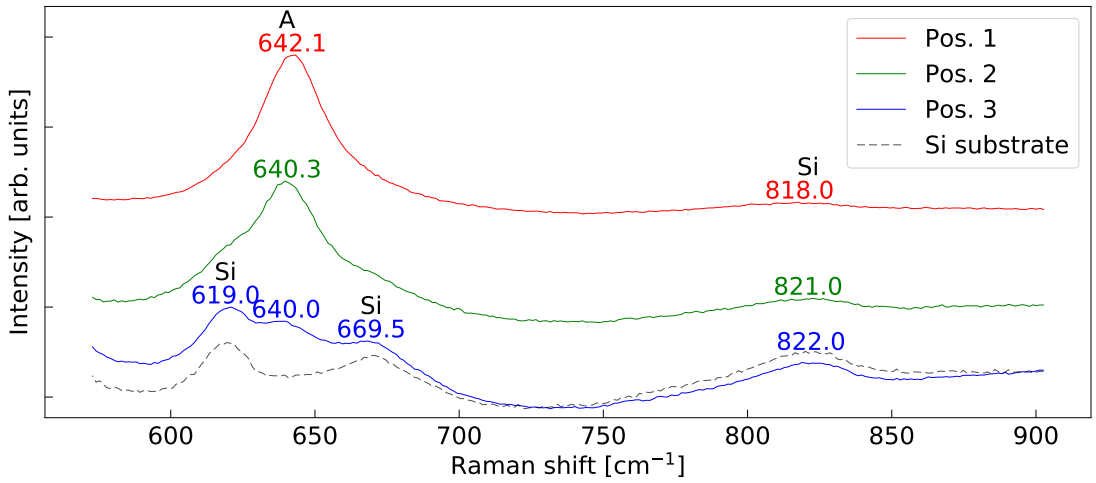

Figure 5.7: Raman spectra from upper spectrum scans in each positions of measurements of the sample PTO700, equally shifted in the y-direction relative to each other, as well as the equivalent scan of the Si substrate for reference. "A" marks anatase peaks, while "Si" marks the silicon peak.

As there is some overlap between some of the peaks in these spectra, especially in pos. 3, WiRE™4 was used to add fitted curves to the same spectra as in figure 5.7, to better illustrate what peaks make up the total measured spectra. This is shown in figure 5.8, with fitted curves shown with dotted lines and the curves still normalised against their most intense peak. It should be noted that the fitted curves of the scan in pos. 3 was chosen to somewhat ignore the part of the spectrum below 600 cm^{-1} and above 850 cm^{-1}, as these "tails" belong to peaks that are outside this part of the spectrum. This was deemed the best way to fit the actual peaks visible. This will however impede on the chi-square value of the curve fitting of this spectrum, and should be noted.

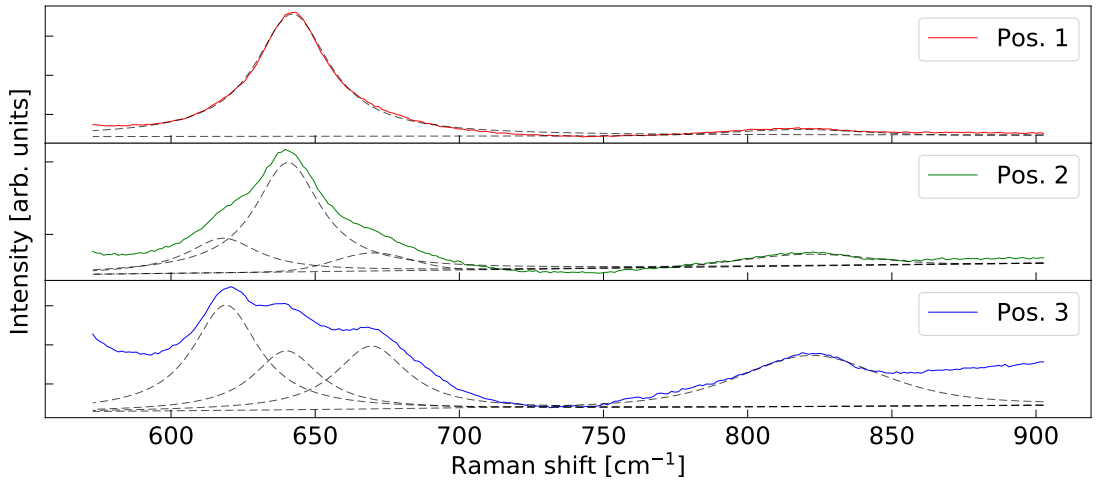

Figure 5.8: Raman spectra from upper spectrum scans in each positions of measurements of the sample PTO700, with each spectrum normalised against the largest peak, and plotted along with fitted curves for each peak.

From the fitted curves, figure 5.8 show the transition between the strong anatase signal in pos. 1, to the spectrum that is the result of a mix between anatase and Si in pos. 3.

The parameters of the fitted curves in figure 5.8 are given in table 5.1. No further studies were conducted using this data, and it is mainly included for transparency and future work, to be proposed in section 5.12. Note that these are the non-normalised values, and as the scan in pos. 3 was conducted with a laser intensity of 50 %, compared to 10 % in pos. 1 and 2, these values can not be compared directly. The intensity values thus represent the number of counts during the measurements. These are usually not given quantitatively when presenting the spectra, but are included here for transparency of the table values.

Table 5.1: Results from curve fitting shown in figure 5.8. All mixed types between Gaussian and Lorentzian. % Gaussian is given, rest is Lorentzian. ChiSq = chi-square value from test for goodness of fit. Values are not normalised.

Pos. (x,y) [μm]	Centre	Width	Height	% Gaussian	Area	ChiSq
Pos. 1	642.1	31.2	31253.0	0.0	1531470.0	17.1
(4202,15637)	818.0	53.0	1554.4	100.0	87636.4	
Pos. 2	618.0	30.0	4761.3	0.0	224369.0	25.2
(4202,-3182)	640.6	27.8	15101.2	0.0	659236.0	
	670.1	30.8	2492.2	100.0	81649.3	
	821.0	51.2	1614.1	100.0	87928.9	
Pos. 3	619.0	28.0	27120.0	0.0	1192800.0	451.9
(4202,-22000)	640.0	28.0	15270.2	0.0	671619.0	
	669.5	30.0	16363.7	5.8	756635.0	
	822.0	60.0	13191.0	45.3	1.061800	

Sample summary

This sample shows clear signs of anatase towards the "plume centre" with noticeable peaks at around 144, 399 and 640 cm^{-1}. Towards the edge of the thin film, the anatase signal becomes weaker and the signal from the Si-substrate "shines through", mainly thought to be caused by the thin film thickness decreasing towards the film edge. A peak shift is also observed between the "plume centre" and the edge of the thin film, likely caused by a strain towards the plume centre, with the major peaks shifting towards 146 and 642 cm^{-1}.

As it was the first sample presented, this sample was analysed in more detail than what will be the case for many of the following samples. Generally, unless the data require a detailed analysis, the following samples similar to this one or any preceding sample will not be as thoroughly analysed, and the reader will in these cases be refereed to the preceding samples with similar results. A summary of similarities in results between the different samples will however be given by the end of this chapter.

5.3 PTO550

This "*plume sample*" is similar to the previous sample PTO700, and therefore have similar results that will not be discussed in too much detail. It shows signs of anatase, but has a weaker signal, which corresponds to the film being thinner than the previous one, as it was grown with fewer pulses.

The measurements were carried out in the the following three positions, given relative to the centre of the wafer, with the flat oriented to the right, as shown in figure 5.9:

- **Pos. 1**: (3250,14700) µm. 'Plume centre'.
- **Pos. 2**: (3250,-2650) µm. 'Midpoint'.
- **Pos. 3**: (3250,-20000) µm. 'Film Edge'.

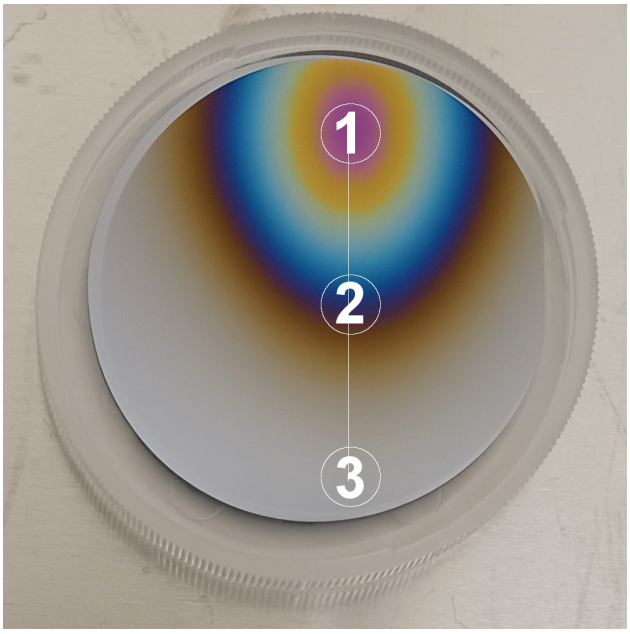

Figure 5.9: Photography of the wafer sample PTO550, and a schematic of the positions of measurement.

Survey scan

Figure 5.10 show the spectra acquired from the survey scan conducted in all positions of measurements on the present sample. It should be noted that there is a generally lower intensity in pos. 3, even from the substrate. The cause of this is not clear, as a drop in signal from the substrate is not expected. It may be because some part of the laser spot was in fact outside the edge of the wafer.

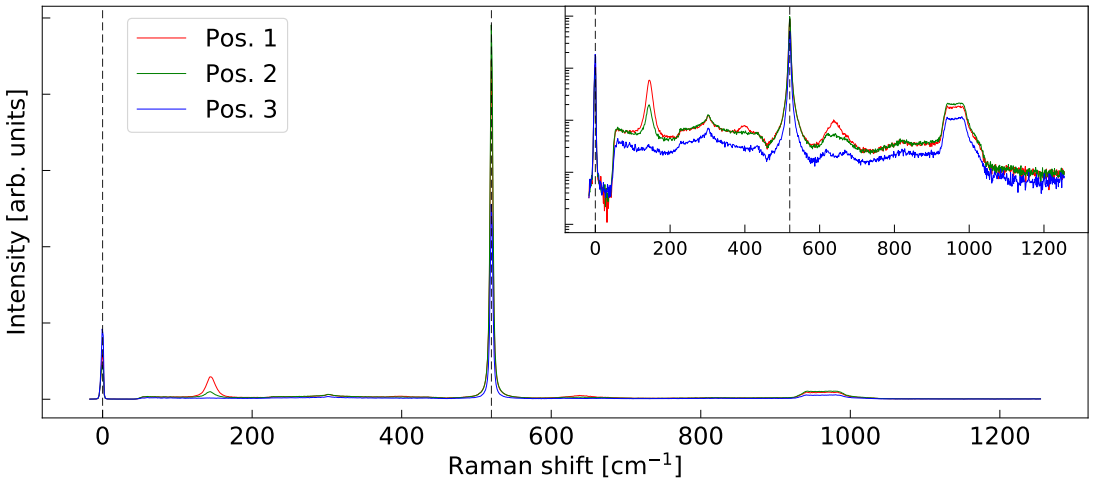

Figure 5.10: Raman spectra from survey scans in each position of measurements of the sample PTO550. Vertical lines mark the Rayleigh-peak at 0 cm^{-1} and the most intense Si-peak 520 cm^{-1}.

Lower spectrum scan

Figure 5.11 show the spectra acquired from the lower spectrum scans conducted in all positions of measurements on the present sample, with annotations marking the peaks in each spectrum. As the scan in pos. 3 was conducted with 50 % laser intensity, all spectra have bean normalised against their tallest peaks, and then bean equally shifted in the y-direction relative to each other. Additional annotations mark which materials the peaks can be attributed to. The spectrum from the equivalent 50 % laser intensity scan of the Si substrate has also been added for reference, normalised to match the corresponding Si peak in the pos. 3 spectrum.

Pos. 2 on this sample has a Raman spectrum that resembles the one in pos. 3 on the previous sample PTO700. In pos. 3 on the present sample the Raman spectrum mostly resembles that of the Si substrate, illustrated by the overlap with the equivalent Si substrate scan, implying that the film is much thinner towards the wafer edge than in the "plume centre". Visual analysis of the sample shown in figure 5.9 can verify this explanation.

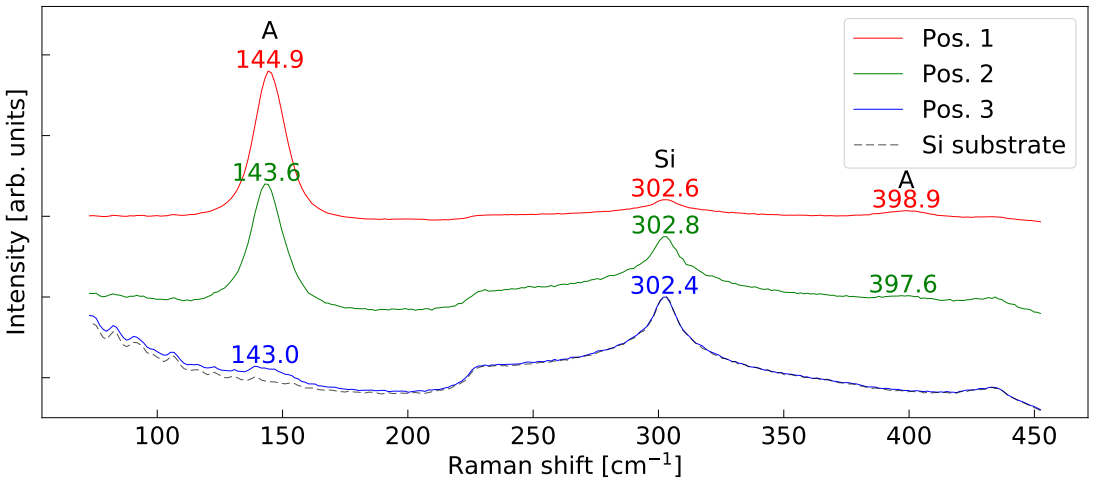

Figure 5.11: Raman spectra from lower spectrum scans in each position of measurements of the sample PTO550, normalised and equally shifted in the y-direction relative to each other, as well as the equivalent scan of the Si substrate for reference. "A" marks anatase peaks, while "Si" marks the silicon peak.

Upper spectrum scan

Figure 5.12 show the spectra acquired from the upper spectrum scans conducted in all positions of measurements on the present sample. Because of weak signals in this part of the spectrum on this sample, all scans were made with 50 % laser intensity. The spectra was still chosen to be plotted after normalisation for continuity within the sample, and to be easier compared to the upper spectrum scans of the previous sample PTO700 in figure 5.7. Additional annotations mark which materials the peaks can be attributed to. The spectrum from the equivalent 50 % laser intensity scan of the Si substrate has also been added for reference, normalised against its most intense peak and shifted to match the lowest value of the scan from pos. 3.

The same trend as mentioned for the lower spectrum scans of the present sample can also be observed in the upper part of the spectrum, where pos. 3 mainly resemble the spectrum of the Si substrate, again illustrated by the overlapping spectrum from the Si substrate scan.

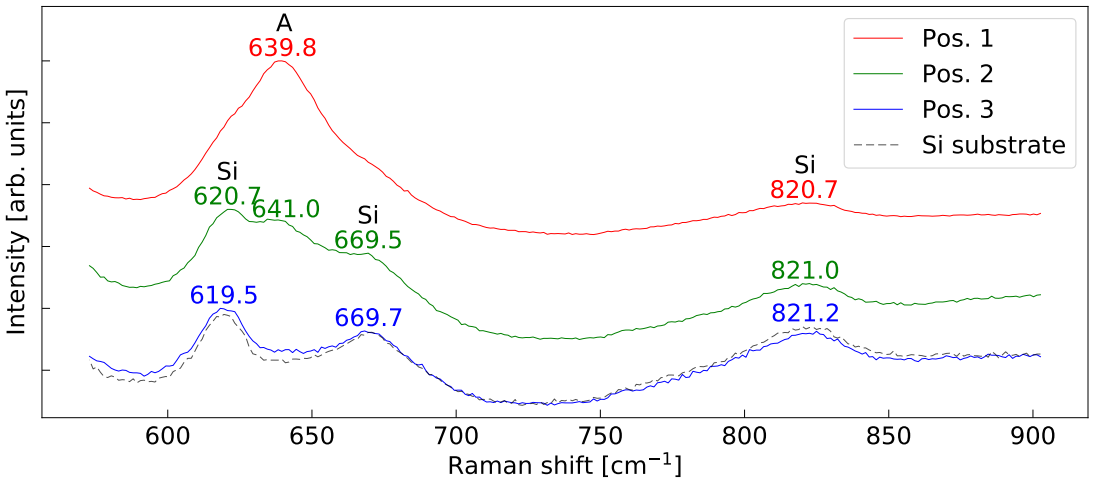

Figure 5.12: Raman spectra from upper spectrum scans in each position of measurements of the sample PTO550, normalised and equally shifted in the y-direction relative to each other, as well as the equivalent scan of the Si substrate for reference. "A" marks anatase peaks, while "Si" marks the silicon peak.

Sample summary

This sample shows clear signs of anatase, with spectra similar to that of the previous sample PTO700. Thus it was not analysed in as much detail. As the only difference is the temperature and the number of pulses, this does make sense.

5.4 PTON550

This sample is mainly differs from the previous sample PTO550 through being deposited with cycling background gas, alternating between O_2 and N_2. Any differences in its Raman data could thus be attributed to the presence of N_2 during deposition. As will be presented, this sample appear to be amorphous TiO_2, with Raman spectra showing broadened peaks that could be attributed to both anatase and rutile. This implies that cycling background gas between O_2 and N_2 during deposition have damaged the crystallinity of the deposited film.

The measurements were carried out in the the following three positions, given relative to the centre of the wafer, with the flat oriented to the right, as shown in figure 5.13:

- **Pos. 1**: (5000,14800) µm. 'Plume centre'.
- **Pos. 2**: (5000,-2600) µm. 'Midpoint'.
- **Pos. 3**: (5000,-20000) µm. 'Film Edge'.

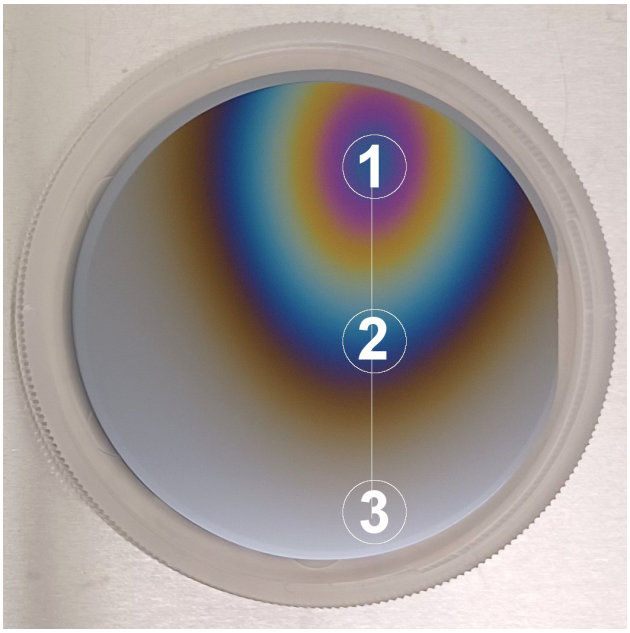

Figure 5.13: Photography of the wafer sample PTON550, and a schematic of the positions of measurement.

Survey scan

Figure 5.14 show the spectra acquired from the survey scans conducted in all positions of measurements on the present sample.

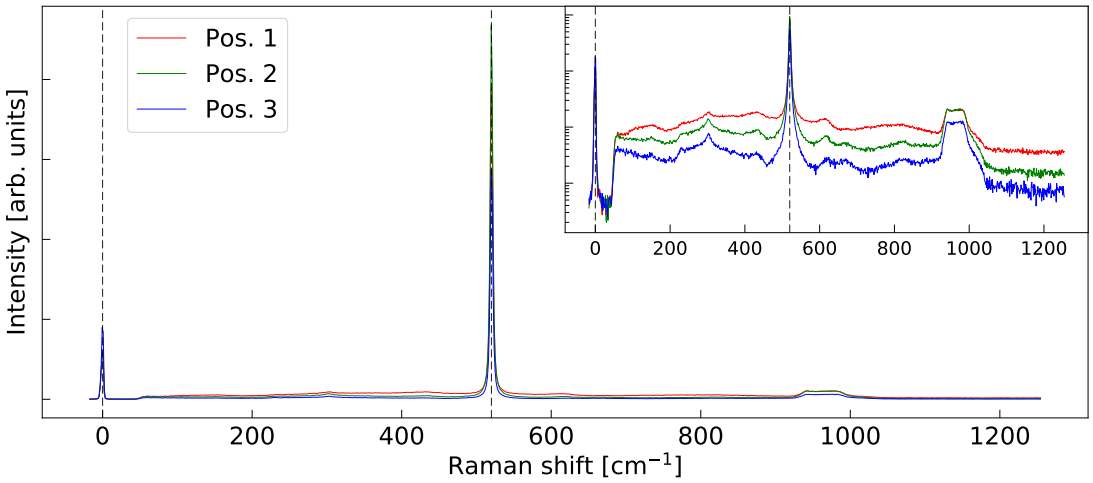

Figure 5.14: Raman spectra from survey scans in each position of measurement of the sample PTON550. Vertical lines mark the Rayleigh-peak at 0 cm^{-1} and the most intense Si-peak 520 cm^{-1}.

Like with the previous sample, PTO550, the present sample shows a general intensity loss towards the wafer edge. This might simply be caused by the decrease in film thickness.

Lower spectrum scan

Figure 5.15 show the spectra acquired from the lower spectrum scans conducted in all positions of measurements on the present sample, with annotations marking the peaks in each spectrum. As all measurements were carried out using the "standard" parameters, i.e. 10 % laser intensity in all positions, the spectra were not normalised for this plot. Equivalent scan of the Si substrate added for reference, like with the previous samples.

While the spectrum in pos. 3 clearly just resembles the spectrum of the Si substrate, the spectrum in pos. 1 is harder to gather clear information from. This spectrum does not resemble a pure anatase spectrum, as with the previous two samples, though the peaks present are not found too far from where one would expect peaks from anatase, at around 144 and 399 cm^{-1} [30, 31, 32]. Rutile should however have peaks around 143 and 447 cm^{-1} [30, 31]. However, because of the general broadening of the peaks in this spectrum, and the increased background signal, this film is believed to be somewhat amorphous, i.e. that the crystallinity of the film has been damaged during deposition because of the cycling of the background gas between O_2 and N_2. Still, the presence of broadened, yet distinct peaks could suggest that the sample has retained some level of crystallinity, which in this case could be a mix between anatase and rutile. A mix of pure crystalline phases should however still show distinct Raman peaks corresponding to each of the crystal phases present.

As the peaks visible in figure 5.15 are not clearly attributed to specific crystal phases, they have only been annotated with their respective centre value.

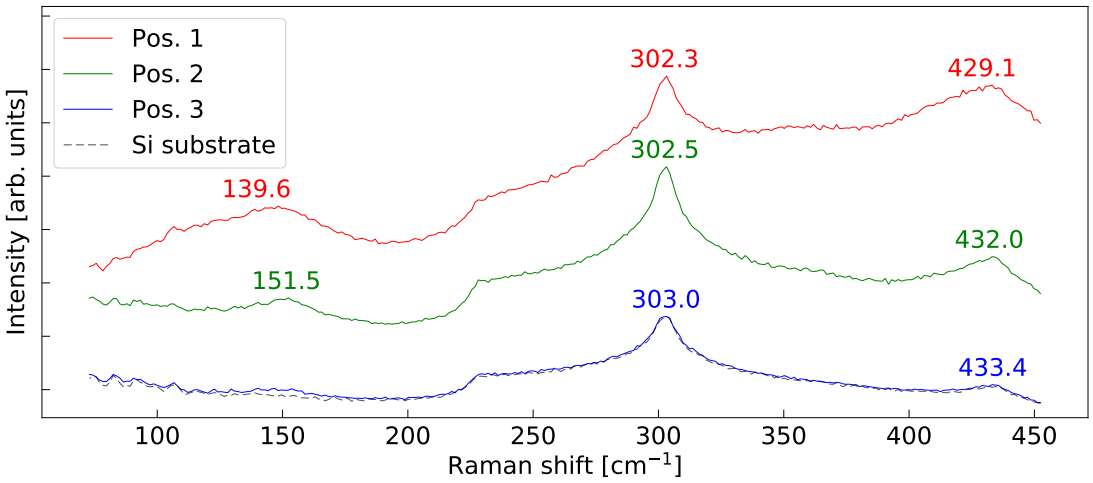

Figure 5.15: Raman spectra from lower spectrum scans in each position of measurements of the sample PTON550, equally shifted in the y-direction relative to each other. Equivalent scan of the Si substrate added for reference.

Upper spectrum scan

Figure 5.16 show the spectra acquired from the upper spectrum scans conducted in all positions of measurements on the present sample. The spectra from both pos. 2 and 3 were obtained using 50 % laser intensity, and so each of the upper scan spectra were plotted after normalisation against their most intense peak. The equivalent scan of the Si substrate is added for reference, like with the previous samples.

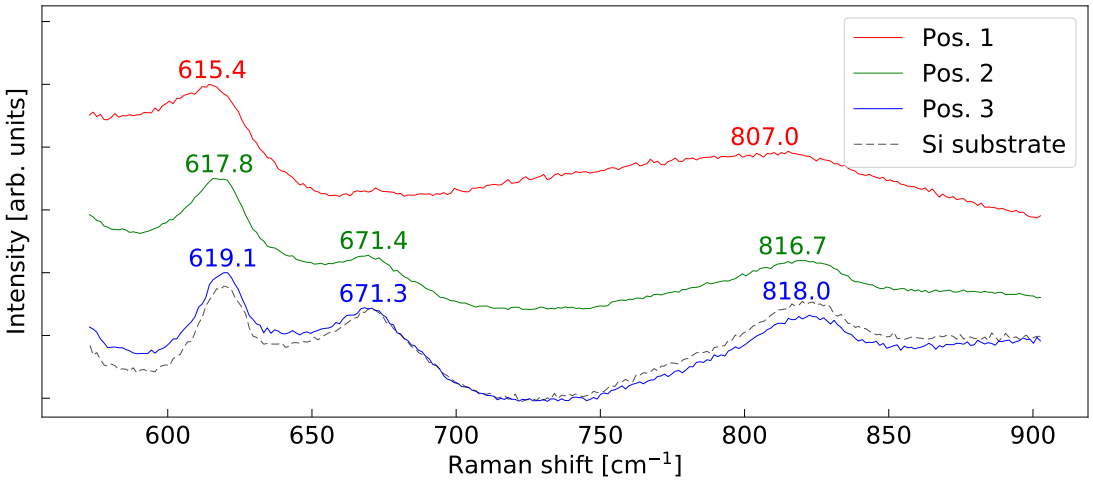

Figure 5.16: Raman spectra from upper spectrum scans in each position of measurement of the sample PTON550, normalised and equally shifted in the y-direction relative to each other. Equivalent scan of the Si substrate added for reference.

A similar trend as in the lower spectrum scan can be observed in the upper spectrum, with broad peaks suggesting that the film is amorphous. Though broadened, the

visible peaks in this upper part of the spectrum is could correspond to rutile, as rutile is expected to have its dominant peak around 612 cm^{-1} [26, 30, 31].

As with the lower spectrum scan, as the peaks are not clearly attributed to specific crystal phases, they have only been annotated with their respective centre value.

Sample summary

From its spectra, this sample appear to consist of amorphous TiO_2, with broadened peaks in the spectra that could still be attributed to both the anatase and rutile phases. Compared to the previous TiO_2 thin films, that were both deposited under pure O_2 background gas and had clear signs of crystalline anatase, this implies that the cycling of the background gas, between O_2 and N_2, damaged the crystallinity of this TiO_2 film during deposition. Exactly why or how this is the case is beyond the scope of this thesis.

5.5 PCO700

This "plume sample" was deposited with a CrN target O_2 background gas, as a reference to the doping. Earlier results obtained by variable angle spectroscopic ellipsometry (VASE) showed that the deposited thin film likely contained Cr_2O_3 (eskolaite), as will be confirmed by the Raman results presented in this section.

As Cr_2O_3 has it's dominant peak around 551 cm^{-1} [27, 35], the upper range scan was extended to 535-900 cm^{-1}. This was however the only sample where this was done.

The measurements were carried out in the the following three positions, given relative to the centre of the wafer, with the flat oriented to the right, as shown in figure 5.17:

- **Pos. 1**: (3500,14500) µm. 'Plume centre'.
- **Pos. 2**: (3500,-2750) µm. 'Midpoint'.
- **Pos. 3**: (3500,-20000) µm. 'Film Edge'.

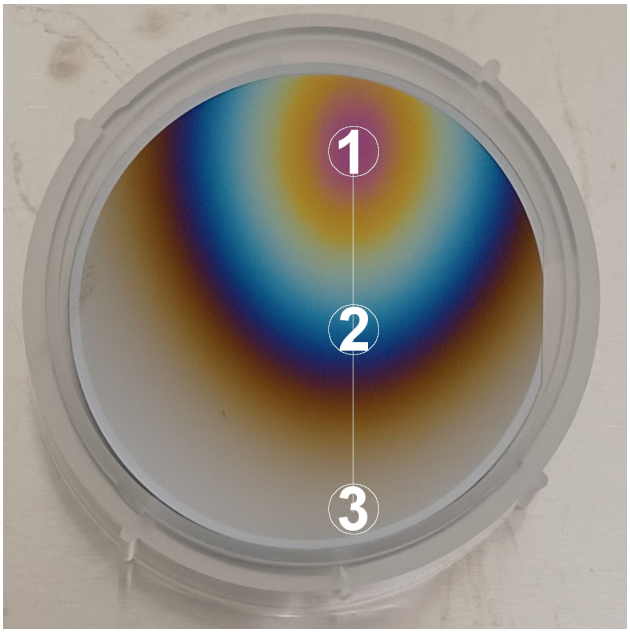

Figure 5.17: Photography of the wafer sample PCO700, and a schematic of the positions of measurement.

Survey scan

Figure 5.18 show the spectra acquired from the survey scans conducted in all positions of measurements on the present sample. One detail that is somewhat unusual, is the fact that the signal appears to be stronger in pos. 2 than in pos. 1. As the thin film should be thickest towards the "plume centre", this was not expected.

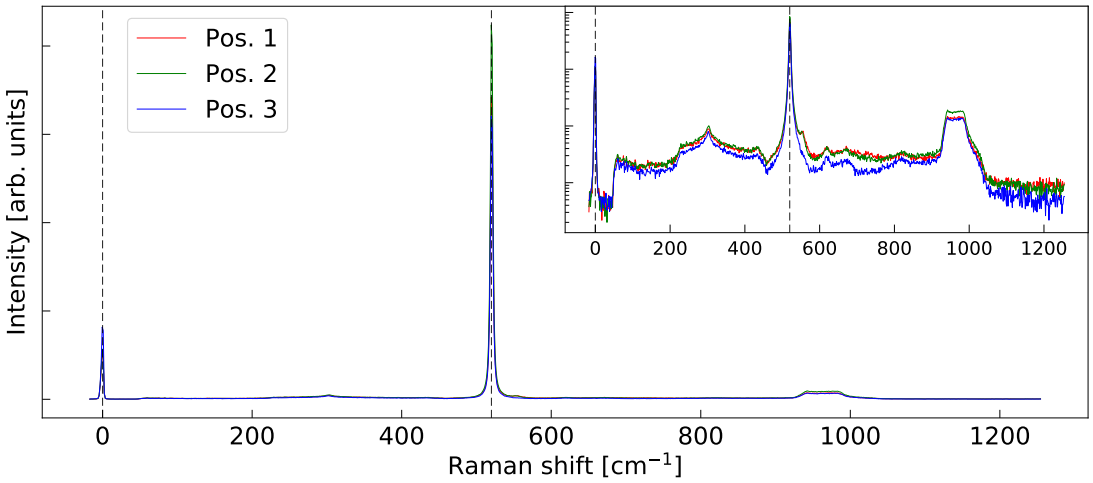

Figure 5.18: Raman spectra from survey scans in each position of measurement of the sample PCO700. Vertical lines mark the Rayleigh-peak at 0 cm^{-1} and the most intense Si-peak 520 cm^{-1}.

Lower spectrum scan

Figure 5.19 show the spectra acquired from the lower spectrum scans conducted in all positions of measurements on the present sample. As all measurements were carried out using the "standard" parameters, i.e. 10 % laser intensity in all positions, the spectra were not normalised for this plot.

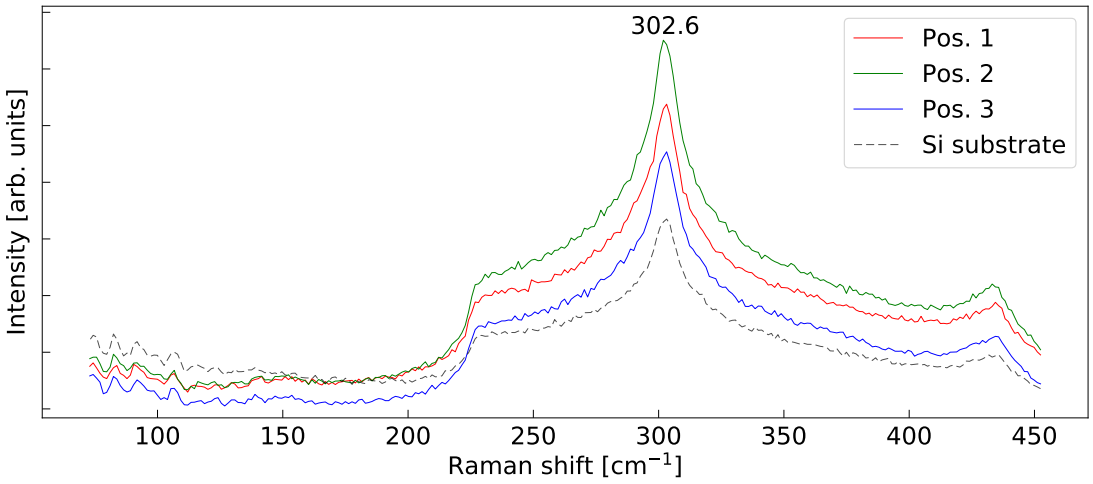

Figure 5.19: Raman spectra from lower spectrum scans in each position of measurements of the sample PCO700, plotted as is without any shift between the spectra. Equivalent scan of the Si substrate added for reference.

As opposed to how the lower spectrum scans of most of the previous samples have been presented, the spectra of figure 5.19 were also plotted without any shift between

the spectra. The equivalent scan of the Si substrate was added for reference, also without any shift or normalisation. This is to show how similar the spectra are, and further show that the signal is stronger in pos. 2 than in pos. 3, which as earlier mentioned is somewhat counter intuitive. These spectra are very similar as they mostly resemble that of the Si substrate, which is to be expected as Cr_2O_3 should not have any significant peaks in this lower part of the spectrum. Thus, only their shared peak is annotated, from the average value of 302.6 cm^{-1} $\pm$ 0.2.

Upper spectrum scan

Figure 5.20 show the spectra acquired from the upper spectrum scans conducted in all positions of measurements on the present sample. The spectra from all positions were obtained using 50 % laser intensity, and are plotted without normalisation. They were however plotted with equal shift relative to each other. Additional annotations mark which materials the peaks can be attributed to.

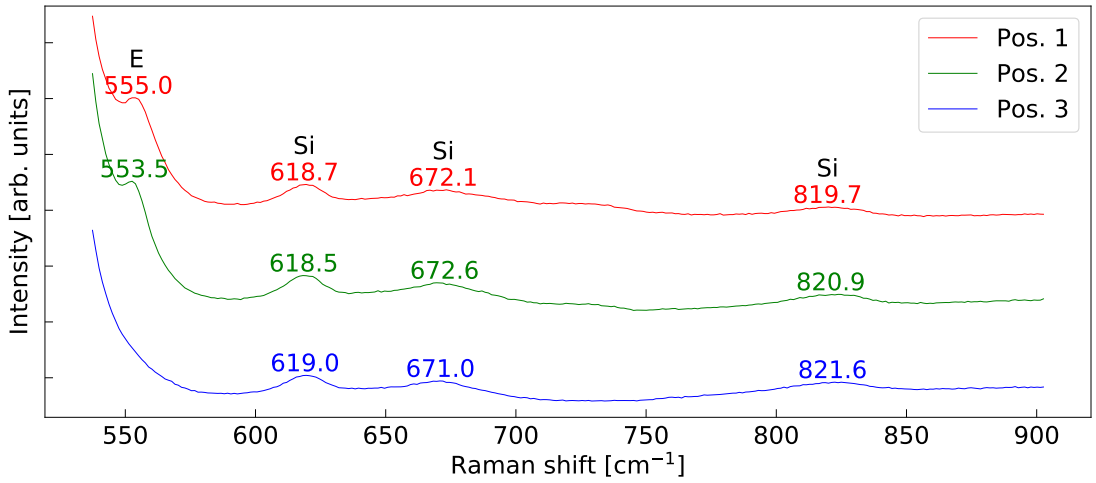

Figure 5.20: Raman spectra from upper spectrum scans in each position of measurement of the sample PCO700, equally shifted in the y-direction relative to each other. "E" marks the eskolaite (Cr_2O_3) peak, "Si" marks silicon peaks.

As previously mentioned, this thin film was expected to contain Cr_2O_3, which has it's dominant peak around 551 cm^{-1} [27, 35]. Thus the upper range scan of this sample was extended to 535-900 cm^{-1}. This did indeed capture the mentioned peak of Cr_2O_3, visible to the left end of the spectrum on the edge of he tail of the 521 cm^{-1}-peak of the Si substrate. This peak also vanishes towards the edge of the thin film, leaving only the spectrum of the Si substrate, as should be expected. The other peaks of Cr_2O_3 are however not clearly observed, and probably disappear in the nearby Si-peaks.

As reference scans of the Si substrate were only obtained with the standard parameters, and thus does not cover the extended part of the range in figure 5.20, it was not added for reference.

Sample summary

The measurements conducted on the present sample successfully verify that the deposited thin film consists of Cr_2O_3, even though it was deposited with a CrN target. The oxidisation of the deposited thin film is thought to be caused by the O_2 background gas pressure.

5.6 PCN550

As opposed to the previous sample PCO700, which was deposited with only O_2 background gas, the present sample was deposited with only N_2. This was with the intent of growing a thin film of only CrN, which is expected to have a Raman spectrum with peaks at 238 and 619 cm^{-1} [33]. This sample did however not show any clear Raman peaks, and as the results from the plume centre were ambiguous, only two positions were measured not to spend too much time on this sample. Thus the measurements were carried out in the the following two positions, given relative to the centre of the wafer, with the flat oriented to the right, as shown in figure 5.21:

- **Pos. 1**: (3500,14500) µm. 'Plume centre'.
- **Pos. 2**: (3500,-20000) µm. 'Film edge'.

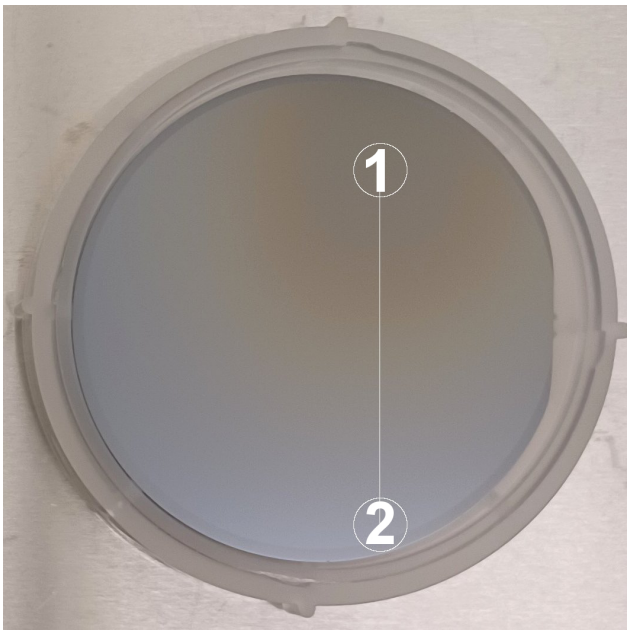

Figure 5.21: Photography of the wafer sample PCN550, and a schematic of the positions of measurement.

Survey scan

Figure 5.22 show the spectra acquired from the survey scans conducted in both positions of measurements on the present sample. It shows that the signal in pos. 1 is very weak. Even the 521 cm^{-1}-peak of Si seams somewhat masked by the CrN thin film. This may imply that the CrN film has reflected the laser light during measurement, which could coincide with the film having a more metallic than semi-conductor quality to it. Still, there is no apparent shift in either peaks.

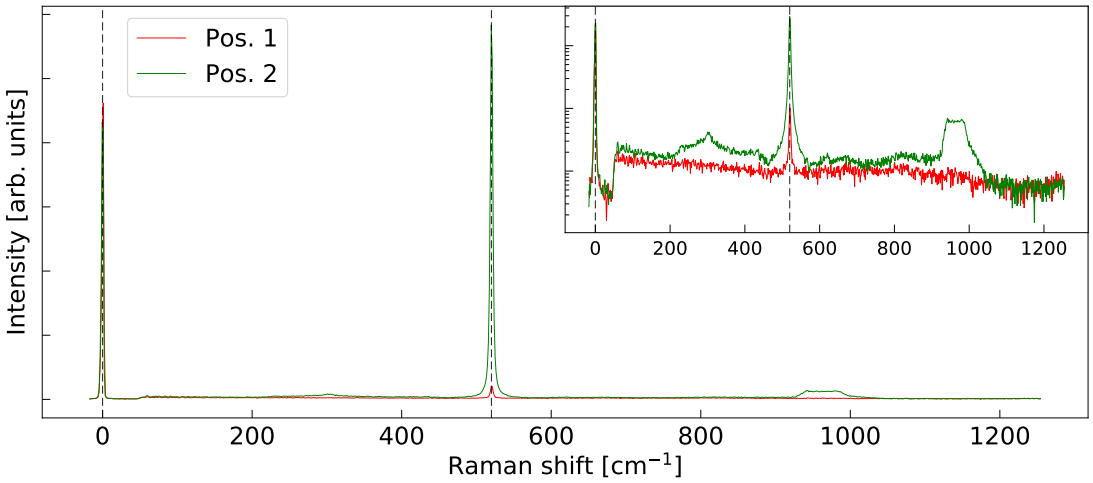

Figure 5.22: Raman spectra from survey scans in each position of measurement of the sample PCN550. Vertical lines mark the Rayleigh-peak at 0 cm^{-1} and the most intense Si-peak 520 cm^{-1}.

Lower spectrum scan

Figure 5.23 show the spectra acquired from the lower spectrum scans conducted in both positions of measurements on the present sample. Both measurements were carried out using the 50 % laser intensity in both positions. Thus, the spectra were not normalised for this plot, nor were they shifted relative to each other to show the weak intensity of the Raman spectrum in pos. 1. The equivalent scan of the Si substrate was added for reference, like with the previous samples.

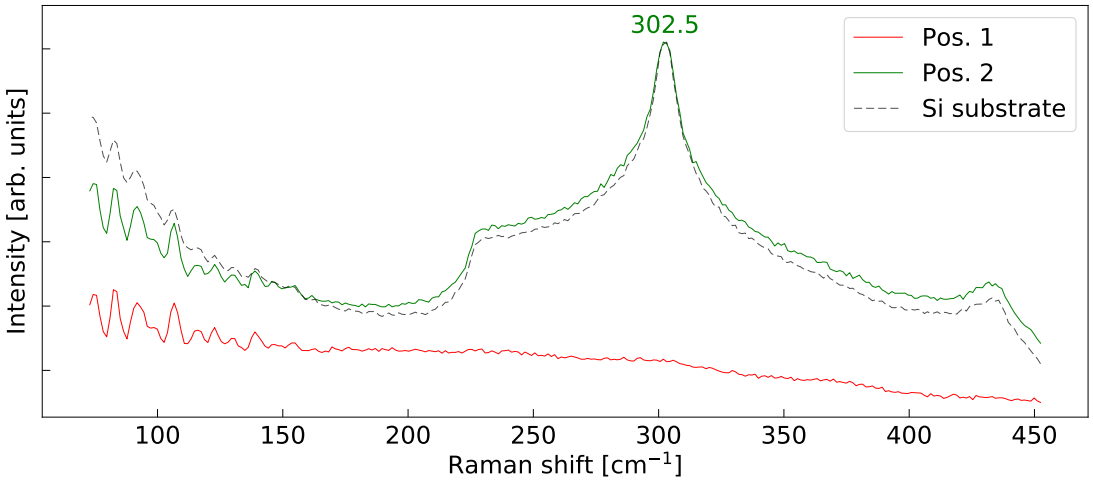

Figure 5.23: Raman spectra from lower spectrum scans in each position of measurements of the sample PCN550, plotted as is without any shift between the spectra. Equivalent scan of the Si substrate added for reference.

While the spectrum from pos. 2 clearly resembles that of the Si substrate, the spectrum obtained from pos. 1, in the "plume centre" of the CrN film, barely have any characteristics or signal at all. As previously mentioned, the Si spectrum seem to have been masked, implying that the CrN film have reflected some of the laser light.

Upper spectrum scan

Figure 5.24 show the spectra acquired from the upper spectrum scans conducted in both positions of measurement on the present sample. Also here, the spectra from both positions were obtained using 50 % laser intensity, and are plotted without normalisation or relative shift, showing that the signal is stronger in pos. 2 in this part of the spectrum as well. The equivalent scan of the Si substrate was again added for reference. Again, the spectrum in pos. 2 resembles that of Si, while the CrN film have a weaker signal and less clearly defined peaks, (though it does appear less "flat" as in the lower spectrum scan).

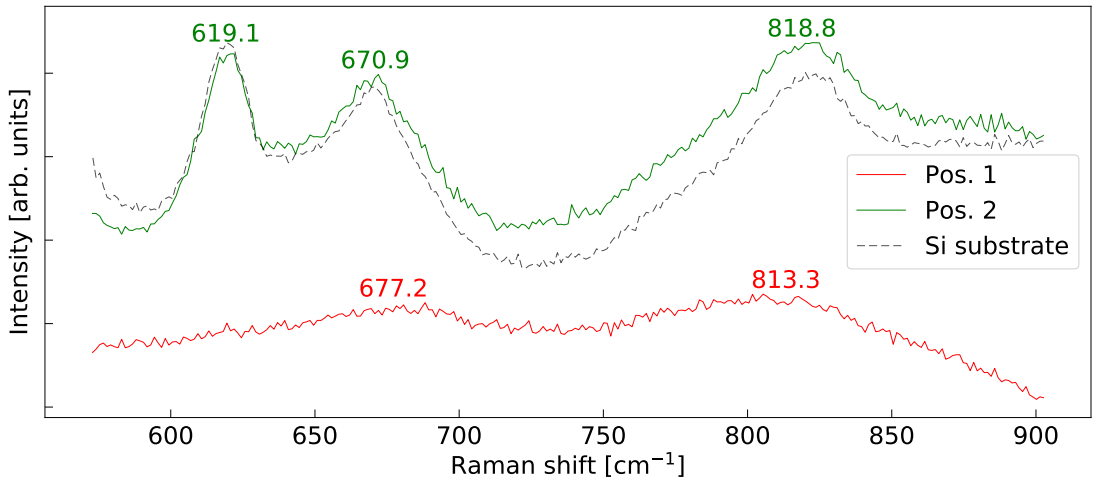

Figure 5.24: Raman spectra from upper spectrum scans in each position of measurement of the sample PCN550, plotted as is without any shift between the spectra. Equivalent scan of the Si substrate added for reference.

Sample summary

There is not much insight to gain from the Raman spectra of this sample, apart from the fact that the CrN film does not provide clear Raman data with well defined peaks. This is however a result in itself, as it implies that the deposited thin film does not contain CrN of any macroscopically ordered crystallinity. Pure CrN should have peaks at around 238 cm^{-1} and 619 cm^{-1} [33]. This is however not observed in the present sample. As the signal from the Si substrate appear "masked" by the film, one could argue that the deposited thin film have reflected the laser. The film thus show metallic qualities, implying that there is no crystalline order to the possible interstitial N, showing a Raman signal more resemblant metallic Cr.

5.7 F0.33,1.63

This, and the next sample, have been categorised as "film samples", as they were both deposited with a rotating substrate.

The present sample was grown with no shift in plume position during deposition, and thus can be compared to the sample PTO700, but deposited with a rotating substrate. Still, this sample show clear signs of anatase.

To monitor the symmetry of the sample, the measurements were carried out in the the following five positions, given relative to the centre of the wafer, with the flat oriented to the right, as shown in figure 5.25:

- **Pos. 1**: (0,0) µm. 'Origo'.
- **Pos. 2**: (0,10000) µm. 'Upper midpoint'.
- **Pos. 3**: (0,-10000) µm. 'Lower midpoint'.
- **Pos. 4**: (0,20000) µm. 'Upper film edge'.
- **Pos. 5**: (0,-20000) µm. 'Lower wafer edge'.

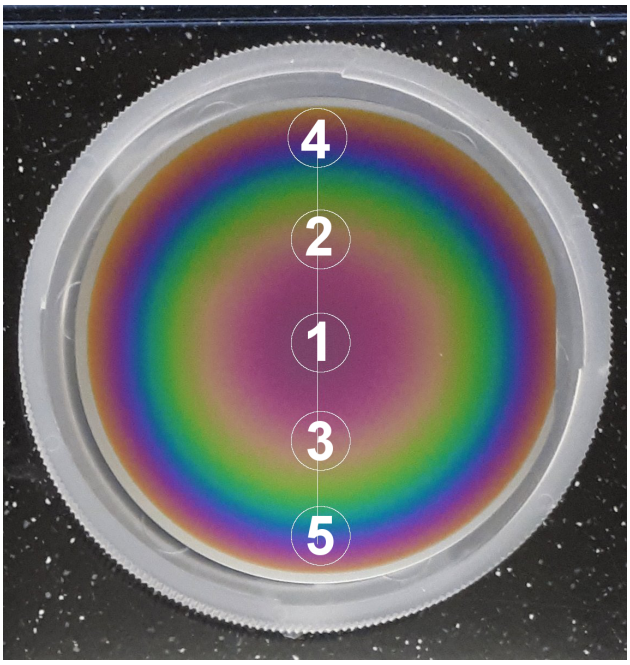

Figure 5.25: Photography of the wafer sample F0.33,1.63, and a schematic of the positions of measurement.

Survey scan

Figure 5.26 show the spectra acquired from the survey scans conducted in all positions of measurement on the present sample. Some differences in intensity are visible, suggesting that the thin film is not equally thick across the sample.

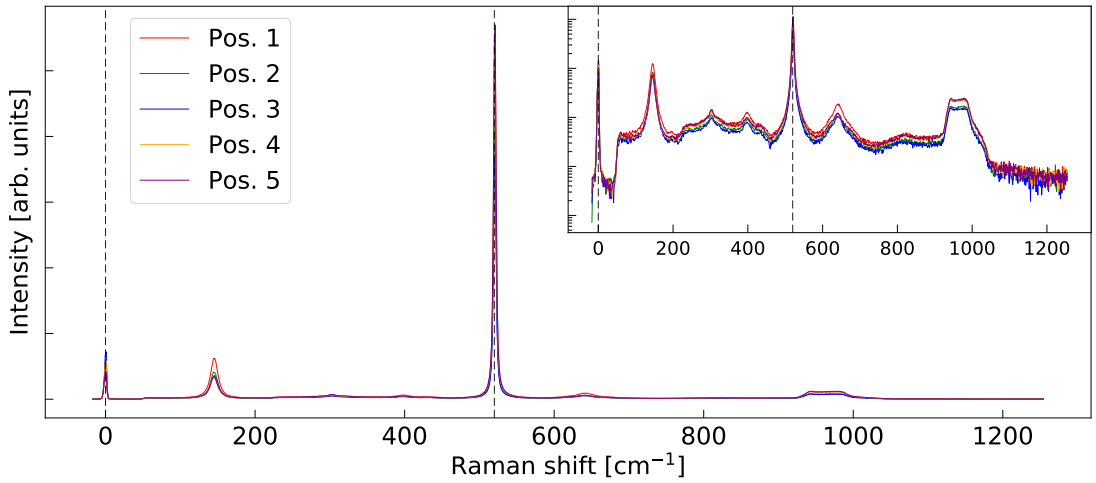

Figure 5.26: Raman spectra from survey scans in each position of measurement of the sample F0.33,1.63. Vertical lines mark the Rayleigh-peak at 0 cm^{-1} and the most intense Si-peak 520 cm^{-1}.

Lower spectrum scan

Figure 5.27 show the spectra acquired from the lower spectrum scans conducted in all positions of measurement on the present sample. All scan were made with standard parameters, i.e. 10 % laser intensity. The spectra were not normalised or shifted, as they are expected to be similar.

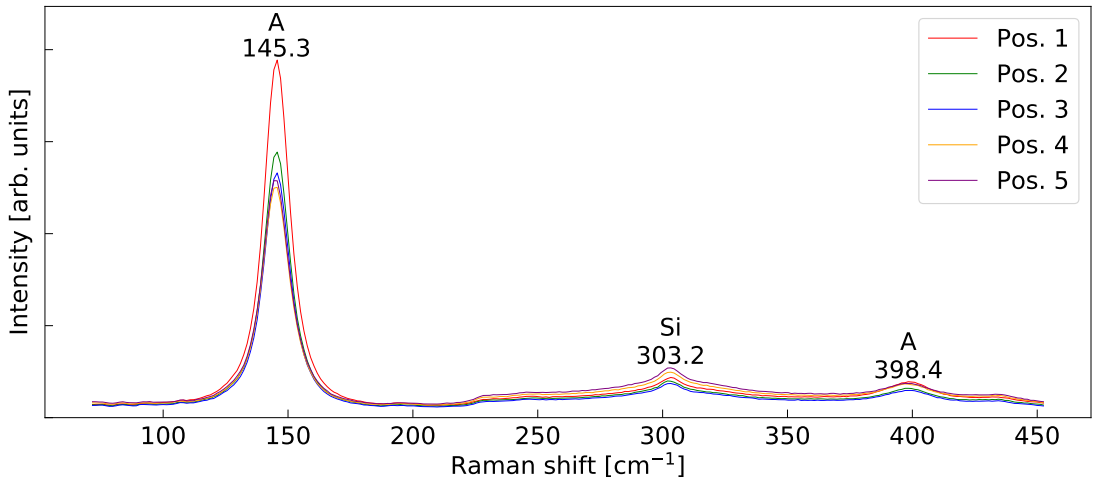

Figure 5.27: Raman spectra from lower spectrum scans in all position of measurement of the sample F0.33,1.63, plotted as is without any shift between the spectra. "A" marks anatase, while "Si" marks silicon.

Little to no shift is observed, and the differences between the spectra are mainly in intensity. This, as previously mentioned is likely caused by differences in thickness

across the sample. As all spectra mainly share the same peaks, the peaks are commonly annotated for all spectra. These peaks, as mentioned for earlier samples, belong to anatase, and the Si substrate. Annotated are the average values with a variance of ± 0.3 or less.

Upper spectrum scan

Figure 5.28 show the spectra acquired from the upper spectrum scans conducted in all positions of measurement on the present sample. Also here, all scan were made with standard parameters, and were plotted without normalisation or shift. This reveals similar trends as for the lower spectrum scans, and so again the peaks are commonly annotated for all spectra.

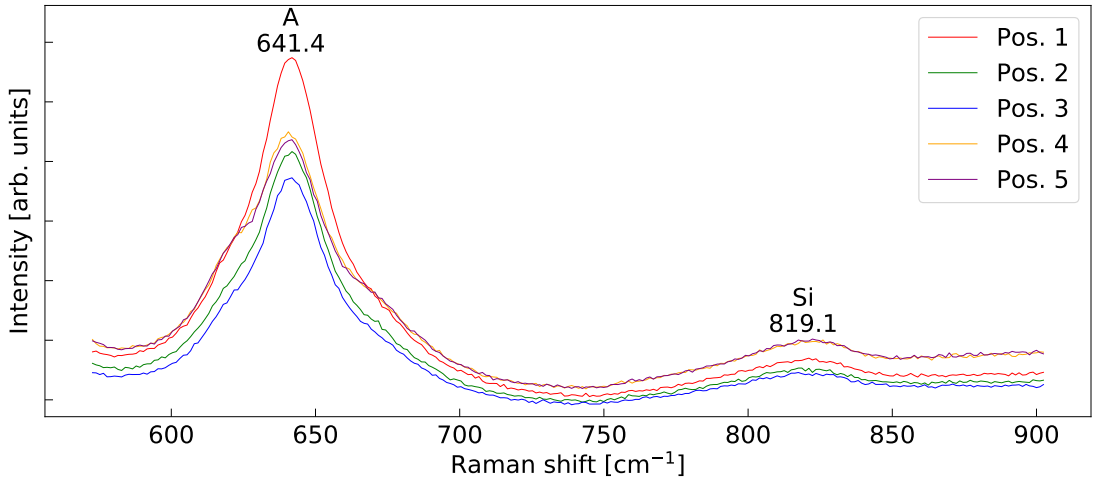

Figure 5.28: Raman spectra from upper spectrum scans in each position of measurement of the sample F0.33,1.63, plotted as is without any shift between the spectra. "A" marks anatase, while "Si" marks silicon.

Annotated are the average values with a variance of ± 0.6 or less. Some "shoulders" become visible on each side of the 641 cm^{-1} peak in pos. 4 and 5. As was shown with curve fitting in figure 5.8 during the presentation of the sample PTO700, these shoulder arrive from the spectrum of the Si substrate as the anatase signal weakens with the decreasing TiO_2 film thickness. This same argument will not be presented again for this sample.

Sample summary

The spectra of the present sample imply that it contains crystalline anatase TiO_2. There are only small variations in the spectra obtained throughout the sample, which was expected as this sample was grown to be a thin film evenly deposited across the substrate. With little variation across the sample, and results similar to the previous TiO_2 plume samples, the present sample will not be discussed in further detail.

5.8 F0.0,3.0

The present sample is very similar to the previous sample F0.33,1.63, and it does also this sample show clear signs of anatase. The only difference in deposition parameters from the previous sample, is that the deposition centre was shifted to 30 mm in the y-direction relative to the wafer centre, i.e. a little bit outside the edge of the substrate wafer. This was to optimise evenness of the thickness of the deposited thin film.

Equally to the previous sample, F0.33,1.63, the measurements were carried out in the the following five positions, given relative to the centre of the wafer, with the flat oriented to the right, as shown in figure 5.29:

- **Pos. 1**: (0,0) µm. 'Origo'.
- **Pos. 2**: (0,10000) µm. 'Upper midpoint'.
- **Pos. 3**: (0,-10000) µm. 'Lower midpoint'.
- **Pos. 4**: (0,20000) µm. 'Upper film edge'.
- **Pos. 5**: (0,-20000) µm. 'Lower wafer edge'.

Figure 5.29: Photography of the wafer sample F0.0,3.0, and a schematic of the positions of measurement.

Through visual analysis of the present sample from figure 5.29, one can verify that it does in fact have a more even thickness than the previous "film sample", F0.33,1.63, simply from the fact that it has less visible interference rings.

As it is very similar to the previous sample, the results will be presented in the same manner.

Survey scan

Figure 5.30 show the spectra acquired from the survey scans conducted in all positions of measurement on the present sample. This reveals little difference in intensity across the sample, as was expected.

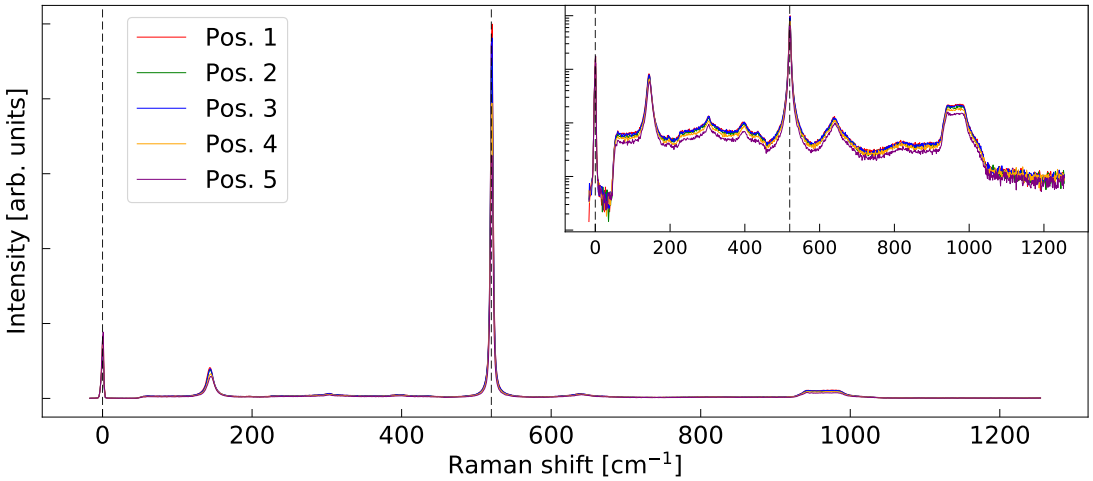

Figure 5.30: Raman spectra from survey scans in each position of measurement of the sample F0.0,3.0. Vertical lines mark the Rayleigh-peak at 0 cm^{-1} and the most intense Si-peak 520 cm^{-1}.

Lower spectrum scan

Figure 5.31 show the spectra acquired from the lower spectrum scans conducted in all positions of measurement on the present sample. As with the previous sample, F0.33,1.63, all scan were made with standard parameters, and the spectra were not normalised or shifted.

The peaks are commonly annotated for all spectra, showing the average values with a variance of $\pm$ 0.9 or less. It should however be noticed that there is some shift observed in the most intense anatase peak, shifting from 143.9 cm^{-1} in the wafer centre to 144.7 and 145.0 cm^{-1} towards the edges. A similar shift is visible in the less intense anatase peak, with values shifting from 396.8 cm^{-1} in the wafer centre to 397.6 and 398.4 cm^{-1} towards the edges. The above mentioned variance can thus partially be contributed to this shift. There is less difference between intensities than in the previous sample, F0.33,1.63, but it does appear to be a more noticeable peak shift across the present sample.

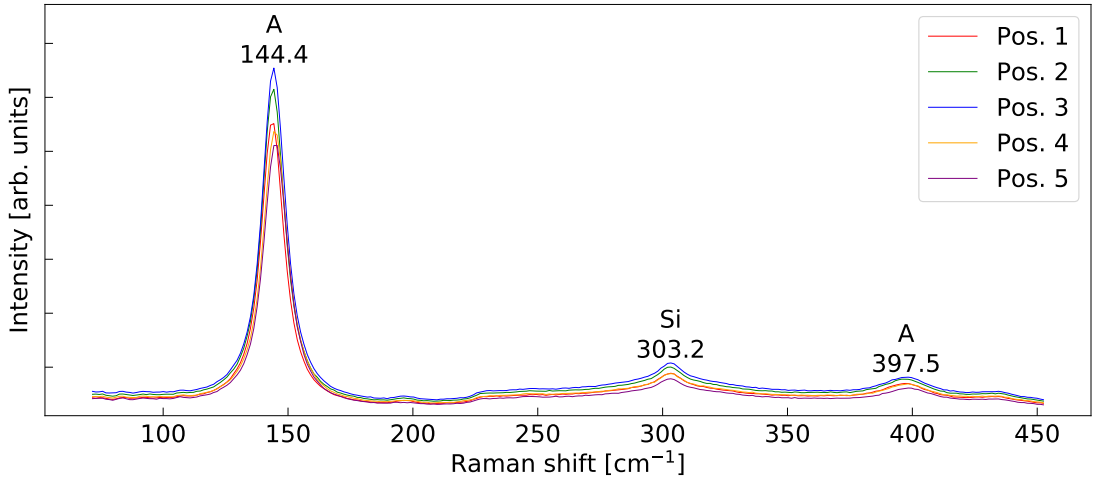

Figure 5.31: Raman spectra from lower spectrum scans in all position of measurement of the sample F0.0,3.0, plotted as is without any shift between the spectra. "A" marks anatase, while "Si" marks silicon.

Upper spectrum scan

Figure 5.32 show the spectra acquired from the upper spectrum scans conducted in all positions of measurement on the present sample. Also here, all scan were made with standard parameters, and were plotted without normalisation or shift. This reveals similar trends as for the lower spectrum scans, and so again the peaks are commonly annotated for all spectra, showing the average values with a variance of $\pm$ 1.1 or less.

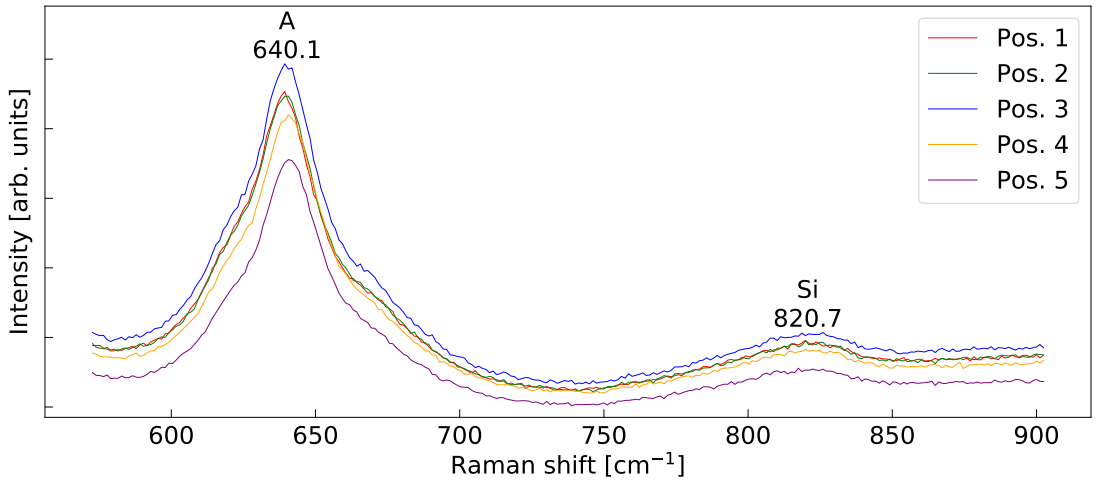

Figure 5.32: Raman spectra from upper spectrum scans in each position of measurement of the sample F0.0,3.0, plotted as is without any shift between the spectra. "A" marks anatase, while "Si" marks silicon.

As with the lower spectrum scans, the upper spectrum scans also reveal some shift

in the anatase peak at around 640 cm^{-1}, shifting from around 639.0 cm^{-1} towards the centre to around 640.8 cm^{-1} towards the edges. This is still not a big shift, though it is more significant than what was obtained from the previous "film sample", F0.33,1.63.

Sample summary

As expected, the present sample is very similar to the previous "film sample", F0.33,1.63, though with more even film thickness across the sample surface, as intended. This can be observed from less variation in both the shape and intensity of the Raman peaks of this sample. This sample does however have a more noticeable shift in the anatase peaks than the previous sample, as will be discussed further in in section 5.11.

5.9 CFRef

Lastly, the two "combinatorial samples" studied will be discussed. This first film was deposited without doping, as a reference sample to CFCrN, the one to follow in the next chapter. This was however still deposited with background gas cycling between O_2 and N_2 in the lower "plume centre", and one could therefore expect trends earlier seen in both the sample PTO550 and PTON550.

The measurements were carried out in the the following three positions, given relative to the centre of the wafer, with the flat oriented to the right, as shown in figure 5.33:

- **Pos. 1**: (0,12000) µm. 'Upper plume centre'.
- **Pos. 2**: (0,0) µm. 'Origo'.
- **Pos. 3**: (0,-12000) µm. 'Lower plume centre'.

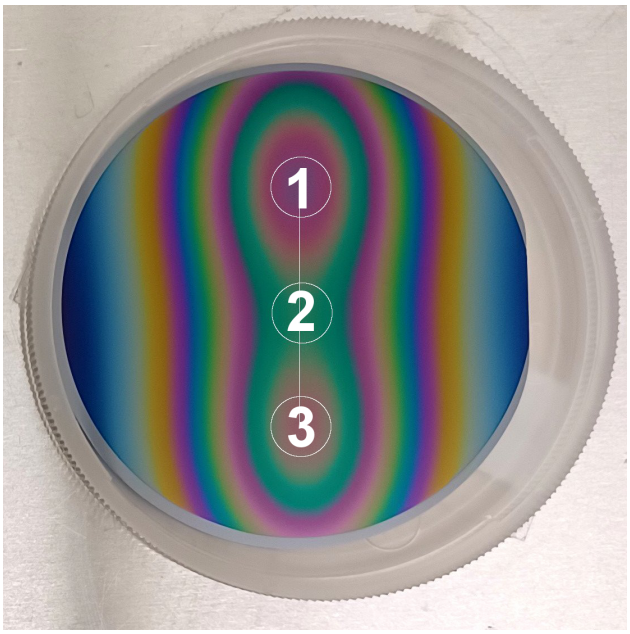

Figure 5.33: Photography of the wafer sample CFRef, and a schematic of the positions of measurement.

If this thin film had been deposited with doping, pos. 3 would be the deposition centre with the highest doping concentration. As this is a reference sample without any doping, pos. 3 was just deposited with pauses during the time that the CrN would otherwise have been deposited. This film is thus expected to be thinner towards pos. 3.

Survey scan

Figure 5.34 show the spectra acquired from the survey scans conducted in all positions of measurement on the present sample. Here, the logarithmic plot show some variation both in intensities and shape of the spectra between the three positions, and the film appear to be amorphous towards pos. 3

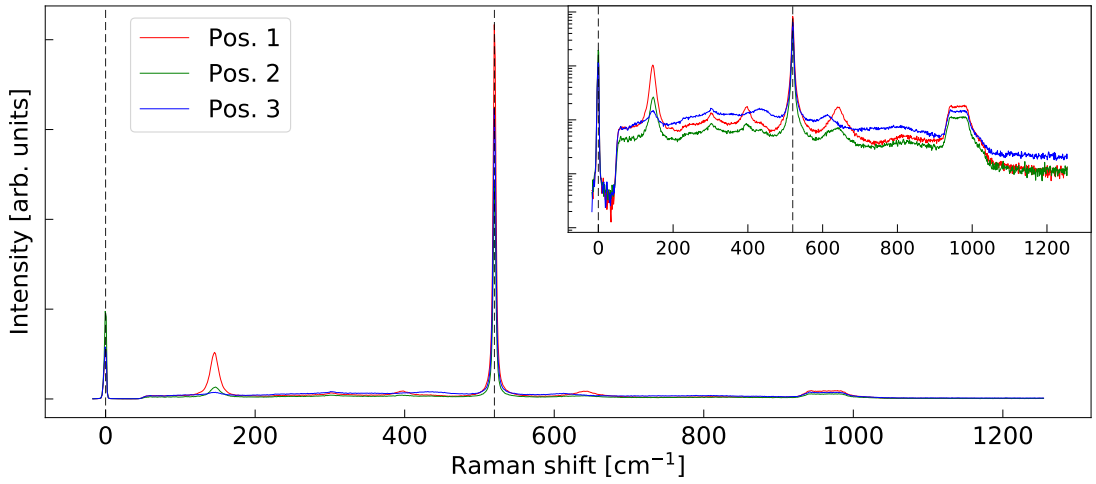

Figure 5.34: Raman spectra from survey scans in each position of measurement of the sample CFRef. Vertical lines mark the Rayleigh-peak at 0 cm^{-1} and the most intense Si-peak 520 cm^{-1}.

Lower spectrum scan

Figure 5.35 show the spectra acquired from the lower spectrum scans conducted in all positions of measurement on the present sample. All scan were made with standard parameters, i.e. 10 % laser intensity. They were still chosen to be presented after normalisation, to better illustrate the different shapes of the spectra. They are also equally shifted in the y-direction.

After normalisation, it is clear that the sample has a spectrum that resembles PTO550, and that the sample contain anatase, in pos. 1, and PTON550 in pos. 3, where the spectrum resembles that of amorphous TiO_2 with some mix between anatase and rutile. This comparison will be made in section 5.11, and corresponds to what was expected for this sample. Thus, a further analysis will not be conducted here, as similar spectra have already been analysed for these previous samples.

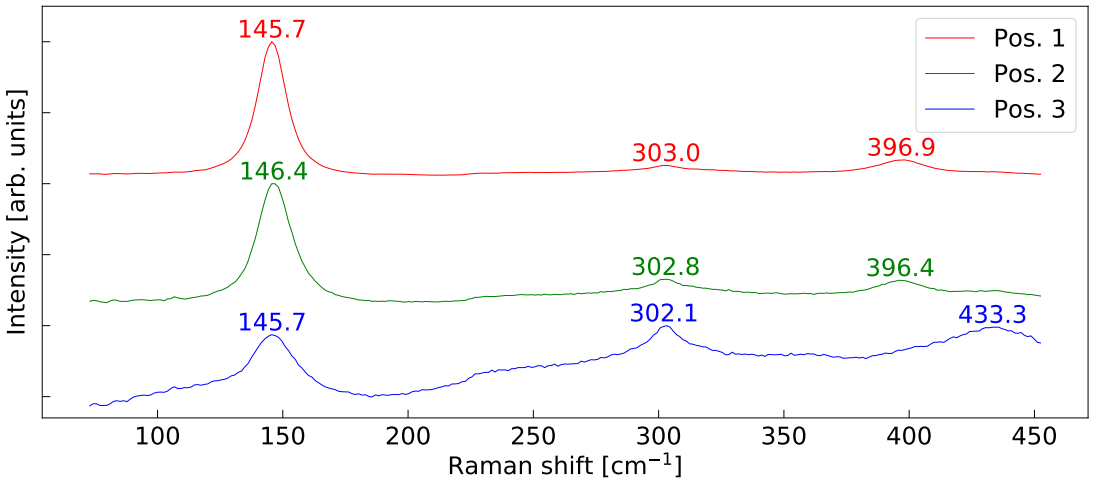

Figure 5.35: Raman spectra from lower spectrum scans in all position of measurement of the sample CFRef, normalised and equally shifted in the y-direction relative to each other.

Upper spectrum scan

Figure 5.36 show the spectra acquired from the upper spectrum scans conducted in all positions of measurement on the present sample. The spectra from both pos. 2 and 3 were obtained using 50 % laser intensity, and so each of the upper scan spectra were plotted after normalisation against their most intense peak.

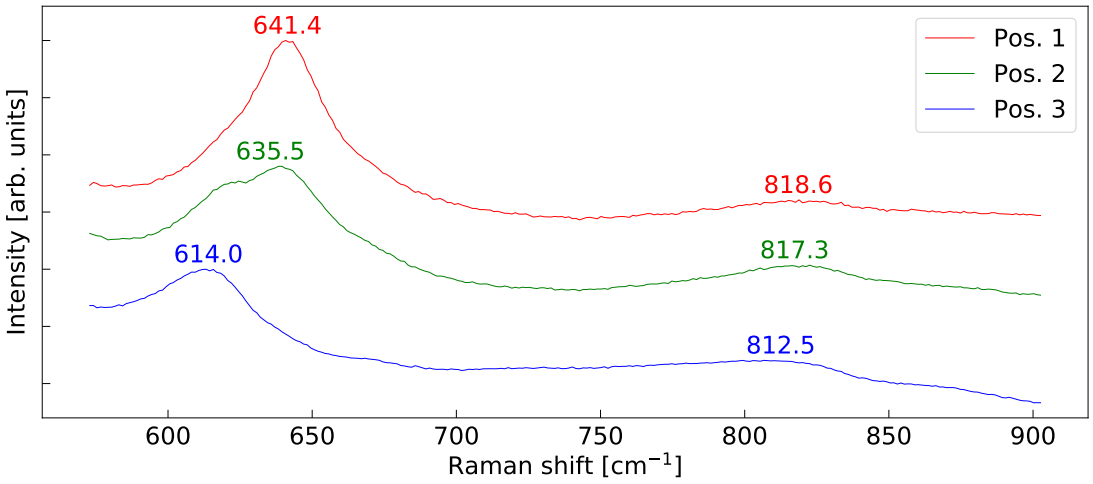

Figure 5.36: Raman spectra from upper spectrum scans in each position of measurement of the sample CFRef, normalised and equally shifted in the y-direction relative to each other.

As expected, and like with the lower spectrum scans, the upper spectrum scans show a spectrum that resembles PTO550 in pos. 1 and PTON550 in pos. 3, while the

spectrum in pos. 2 looks like a mix between the two. Still, the most intense peak in pos. 2 has been annotated with the centre of the total peak.

Sample summary

As expected, the present sample has a spectrum that resembles PTO550 in pos. 1 and PTON550 in pos. 3, while pos. 2 appear as a mix between the two. I.e., the crystalline TiO_2 structure moves from a more pure anatase in pos. 1 to amorphous TiO_2 in pos. 3. This transition towards amorphous TiO_2 is, as previously mentioned during the analysis of the sample PTON550, likely caused by the cycling between O_2 and N_2 background gas during deposition in this position.

5.10 CFCrN

This last sample is similar to the previous sample CFRef, but with actual doping.

The measurements were carried out in the the following three positions, given relative to the centre of the wafer, with the flat oriented to the right, as shown in figure 5.10:

- **Pos. 1**: (-1000,11500) µm. 'Upper plume centre'.
- **Pos. 2**: (-1000,0) µm. 'Midpoint'.
- **Pos. 3**: (-1000,-11500) µm. 'Lower plume centre'.

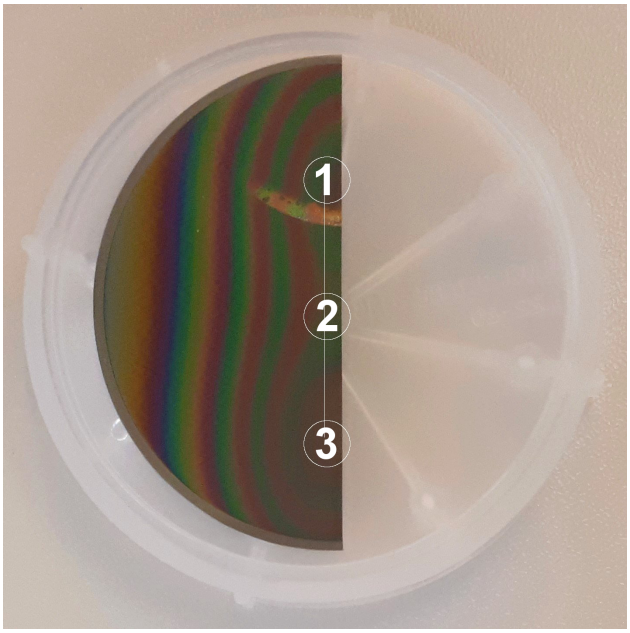

Figure 5.37: Photography of half of the wafer sample CFCrN, and a schematic of the positions of measurement.

From figure 5.37 it is noticeable that the film have bean harmed, causing a line by the upper "plume centre". This was likely caused by the sample getting pinched by the sample box, probably not too long after deposition. The measurement in pos. 1 was however made sure to be far enough from this scarring. This sample was also cleaved in half before the present measurements were conducted, as it was studied for other projects as well, both before and parallel to this master project.

Pos. 3 is the deposition with the highest doping concentration, though CrN should be present across the entire sample. Like with the previous sample, both of the deposition centres in this sample can be expected to resemble the "plume centre" of the "plume samples" with equal growth parameters. Thus, pos. 1 of this sample is expected to resemble PTO550 or PTON550, while pos. 3 is expected to resemble a mix between PTON550 and PCN550 because of the cycling of the background gas and the doping.

Survey scan

Figure 5.38 show the spectra acquired from the survey scans conducted in all positions of measurement on the present sample. The logarithmic plot show variation both in intensities and shape of the spectra between the three positions, especially between pos. 3 and the two ther positions.

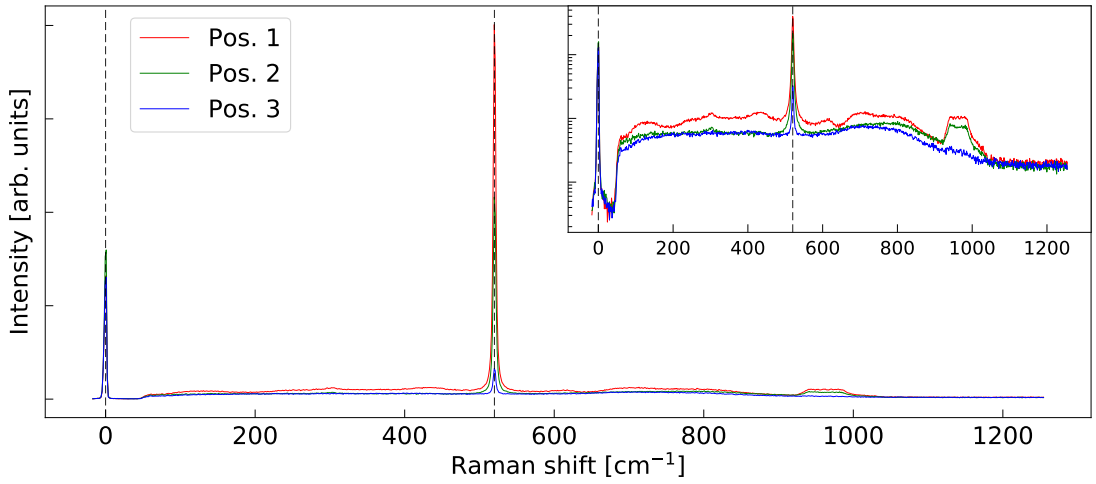

Figure 5.38: Raman spectra from survey scans in each position of measurement of the sample CFCrN. Vertical lines mark the Rayleigh-peak at 0 cm^{-1} and the most intense Si-peak 520 cm^{-1}.

Lower spectrum scan

Figure 5.39 show the spectra acquired from the lower spectrum scans conducted in all positions of measurement on the present sample. All scans were made with 50 % laser intensity. They were still chosen to be presented after normalisation, to better illustrate the different shapes of the spectra. They are also equally shifted in the y-direction.

This sample actually has a spectrum that resembles PTON550 in pos. 1, though with some shift observed in the peaks. This will be compared an discussed further during section 5.11. The spectrum in pos. 3 on the other hand, somewhat resembles that of PCN550, with no clear peaks are visible, and thus no peaks have been annotated. Only one peak is visible in pos. 2, though, as previously shown, this peak originates from the Si substrate.

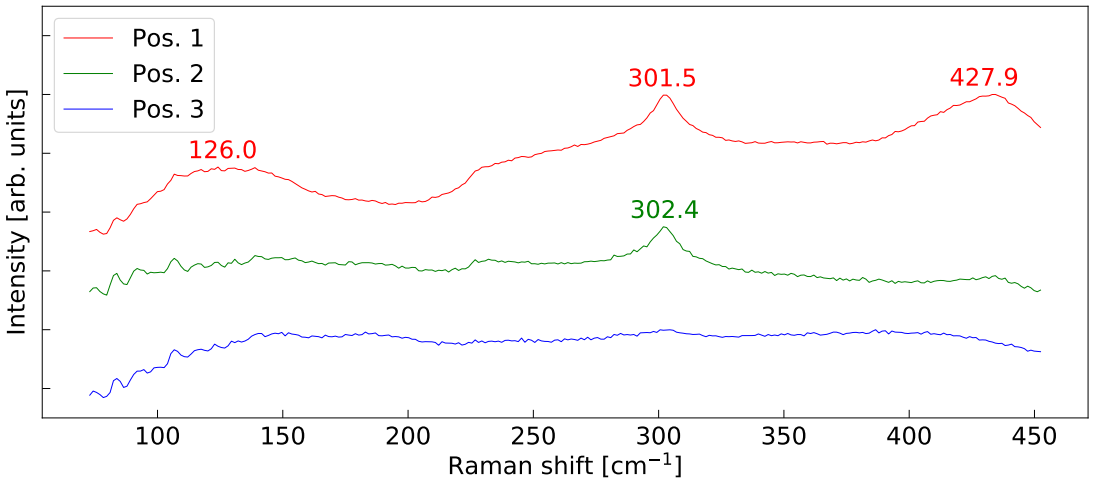

Figure 5.39: Raman spectra from lower spectrum scans in all position of measurement of the sample CFCrN, normalised and equally shifted in the y-direction relative to each other.

Upper spectrum scan

Figure 5.40 show the spectra acquired from the upper spectrum scans conducted in all positions of measurement on the present sample. As with the lower spectrum scans, all scans were made with 50 % laser intensity, but were still chosen to be presented after normalisation, to better illustrate the different shapes of the spectra. They are also equally shifted in the y-direction.

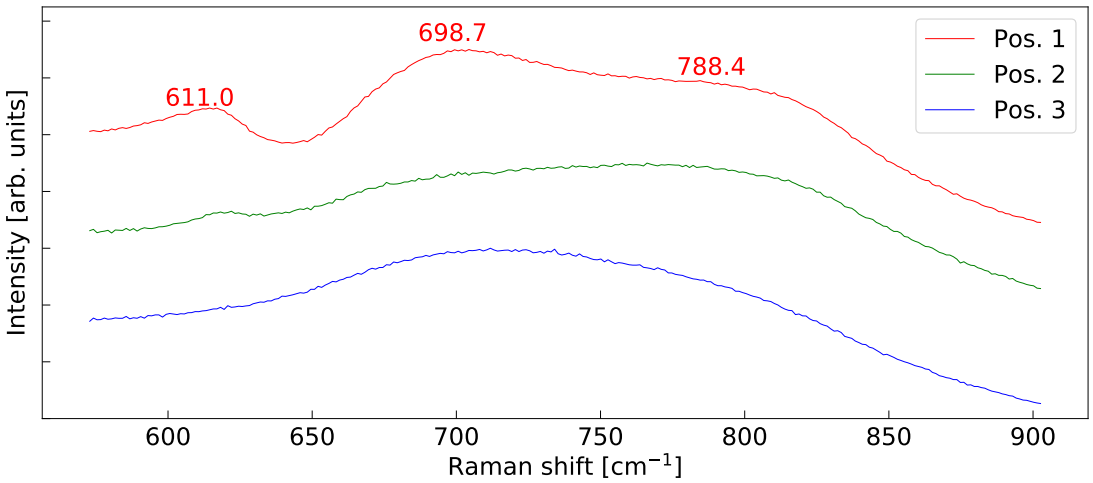

Figure 5.40: Raman spectra from upper spectrum scans in each position of measurement of the sample CFCrN, normalised and equally shifted in the y-direction relative to each other.

Both pos. 2 and 3 appear as mostly amorphous, and the spectrum in pos. 3 still resembles PCN550. The spectrum obtained in pos. 1 is however not fully similar

to the equivalent scan from PTON550, or any of the previous samples. The first peak in pos. 1 is attributed to the dominant peak of rutile, that should be around 612 cm^{-1} [26, 30, 31], though the spectrum still imply that film is mostly amorphous in this position. The rest of the peaks are thus harder to identify, as they do not clearly match any of the expected peaks from the deposited materials, and because of the amorphousness of the deposited thin film. The peak centres in pos. 1 were found using curve fitting. This is shown in in figure 5.41, with the corresponding parameters of the fitted curves given in table 5.2. This spectrum and the data of its fitted curves will however not be analysed in more detail.

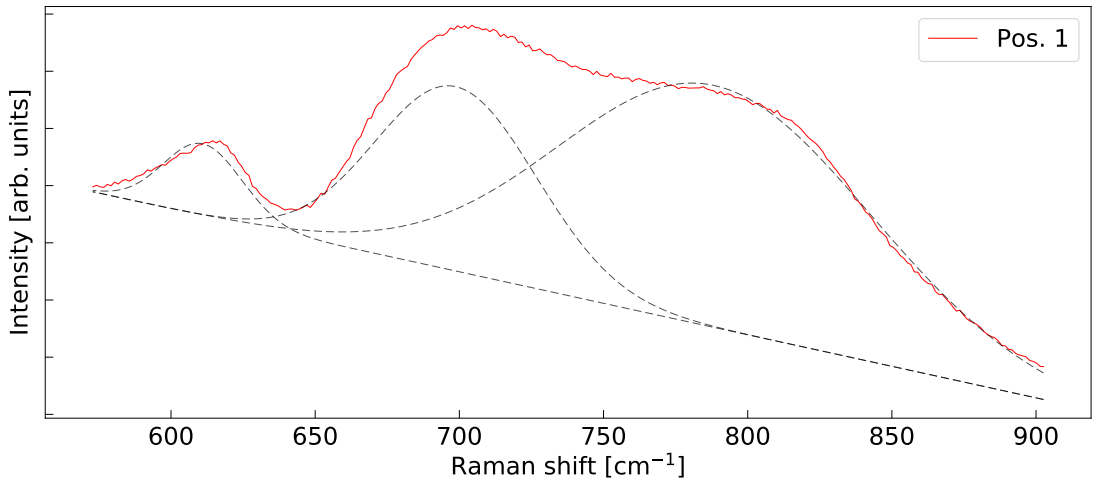

Figure 5.41: Raman spectrum from upper spectrum scans in pos. 1 of the sample CFCrN, plotted with fitted curves.

Table 5.2: Results from curve fitting shown in figure 5.41. All mixed types between Gaussian and Lorentzian. % Gaussian is given, rest is Lorentzian. ChiSq = chi-square value from test for goodness of fit. Values are not normalised.

Pos. (x,y) [µm]	Centre	Width	Height	% Gaussian	Area	ChiSq
Pos. 1	611.0	32.2	12594.6	100.0	431787.0	12.3
(-1000,11500)	698.7	65.8	32252.3	100.0	2260480.0	
	788.4	127.8	42331	100.0	5759300.0	

Sample summary

This last sample has shows signs of a crystalline structure in pos. 1, that rapidly moves towards a more amorphous structure towards pos. 2 and 3, i.e. with increasing doping. The spectra are not equal, but do not contain any features that are detailed enough for any further analysis to be conducted. One can speculate whether the film is completely amorphous or if it might actually be nano-poly-crystalline. This fine distinction is however not detectable with micro-Raman microscopy, at least not without very sophisticated analysis that goes beyond the scope of this thesis.

The spectra obtained from pos. 1 does not match the spectra from pos. 1 of the reference sample, where the deposition parameters where equal, verifying that there is doping in this part of the sample as well, causing this part of the film to be amorphous. This shows that the doping largely affects the crystallinity of the deposited TiO_2 [36].

5.11 Data compilation and sample comparison

This section will provide the reader with an overview of the results presented during this chapter, and compare the data of the samples showing similar trends, to give a better understanding of how the different growth parameters affect the deposited film.

The equipment was deemed stable and well calibrated across the entirety of the conducted measurements, as no systematic variation in either the Rayleigh peak or dominant Si-peak, at 0 and 520 cm^{-1} respectively, was observed. Some random variations do occur, suggesting that the obtained results have an uncertainty of around ± 0.1 cm^{-1}.

Anatase film comparison

Figure 5.42 show a comparison of the films that had clear anatase spectra, comparing the "plume centre" of the "plume samples" PTO700 and PTO550, the wafer centre of the two plume samples, and the upper "plume centre" (without doping or gas cycling) of the combinatorial reference sample CFRef. In the case of CFRef, a shift towards an amorphous phase was observed towards its lower "plume centre" in pos. 3, where the film was deposited with cycling background gas, but sill without any doping, while the other samples presented in figure 5.42 all showed signs of anatase across the entirety of the film. As the "plume samples" have a large thickness gradient across the samples, the signal from the Si substrate did however become stronger away from the "plume centre", as the films became thinner.

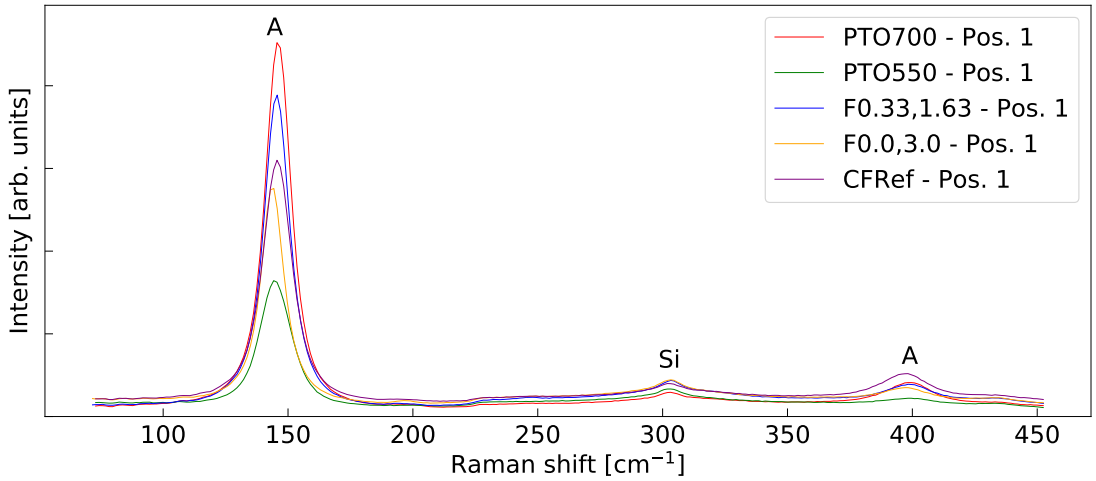

Figure 5.42: Raman spectra from lower spectrum scans of samples with clear anatase content.

Both the "plume samples" grown with TiO_2 and O_2 background gas only, i.e. PTO700 and PTO550, and both the film samples F0.33,1.63 and F0.0,3.0, only showed signs of anatase across the sample. As these samples also showed a shift in peak values across the sample, and as only the mean peak values were plotted for the film samples,

figure 5.43 shows the shift in the dominant anatase peak from the reference value of 144 cm^{-1}, plotted as a function of distance from the deposition centre ("plume centre") of the sample.

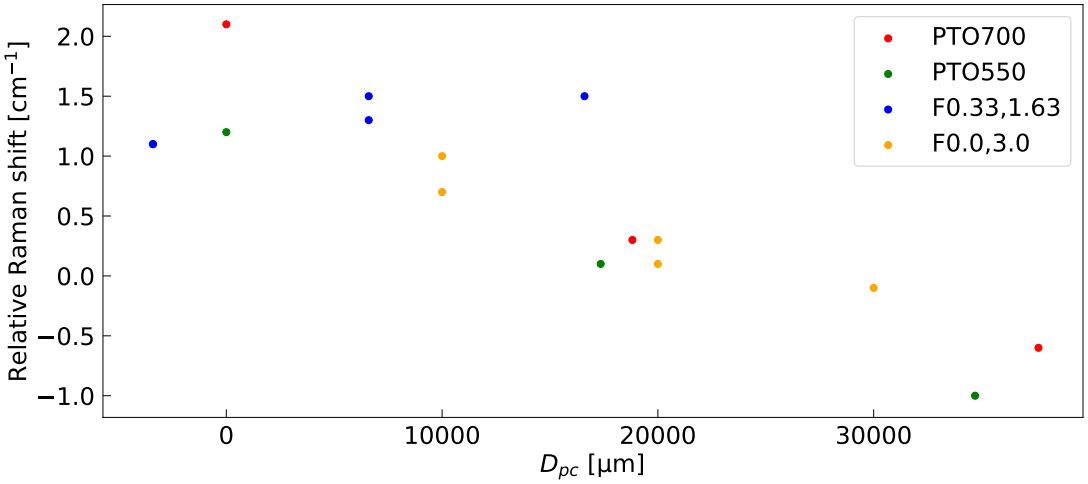

Figure 5.43: Relative Raman shift in the dominant anatase peak from the reference value of 144 cm^{-1}. D_{pc} = distance from the "plume centre" of each sample.

For the "plume samples", the "plume centre" is defined from the measurements. The "plume centre" of the "film samples" is defined from the intended deposition "plume centre" from the PLD parameters, as these have radial symmetry, and no visible "plume centre". According to the data from the PLD process, the deposition centre was set to be at $x = 3.3$ mm and $y = 16.3$ mm for the sample F0.33,1.63, and $x = 0.0$ mm and $y = 30.0$ mm for the sample F0.0,3.0 (hence the sample names), both with an uncertainty of around ± 0.5 mm. Both these samples were deposited while rotating the substrate. The "plume centre" will thus be assumed to be at a radial distance of $\sqrt{3.3^2 + 16.3^2}$ mm ≈ 16.6 mm from the wafer centre for the sample F0.33,1.63, and 30 mm from the wafer centre for the sample F0.0,3.0, both having radial symmetry. The distance from the "plume centre" will thus be radially defined for the "film samples", with the positive direction defined towards the wafer *centre*. The distance from the "plume centre" of each sample is assigned the variable D_{pc}.

From figure 5.43 it is illustrated that there is shift a positive peak shift towards the plume centre. This somehow correlates with the films being thicker towards the plume centre, though F0.0,3.0, which is almost even in thickness across the sample, still has a positive shift towards the "plume centre". The other film sample, F0.33,1.63, is the only sample not completely following this trend. This sample is however not evenly thick, with a thickness variation that does not follow the distance from the "plume centre", but rather a centrosymmetric thickness variation, where the film is thickest towards the wafer centre, because of its non-optimised, rotational deposition. Here, the shift is to a larger degree attributed to the film thickness rather than the distance from the "plume centre".

As the obtained results have an uncertainty of around ± 0.1 cm^{-1}, the observed peak shifts, illustrated in figure 5.43, are well outside this uncertainty. Additionally, these peak shifts mostly follow similar trends. These shifts are attributed to variations in

strain across the films [30, 32]. This strain does however not clearly decrease as the film thickness increases, suggesting that the films could be metastable, or at least that they have not reached a critical thickness of relaxation. This can be attributed to the PLD process, and the fact that this process does not deposit films under thermodynamic equilibrium.

Amorphous and mixed phase film comparison

Lastly, the amorphous spectra that could not be attributed to any pure crystal phases, but still contained some visible peaks, will be compared. Figure 5.44 show the lower scans of these spectra plotted together, comparing the "plume centre" of the "plume sample" PTON550 (with cycling background gas between O_2 and N_2), the lower "plume centre" (with gas cycling, but without doping) of the combinatorial reference sample CFRef, and the upper "plume center" of the combinatorial sample CFCrN, where the lower "plume centre" (pos. 3) was deposited with gas cycling and doping, and thus the upper "plume centre", though deposited without gas cycling or doping, should sill contain some doping from the other "plume centre". The spectra have been normalised against their shared Si peak around 303 cm^{-1}.

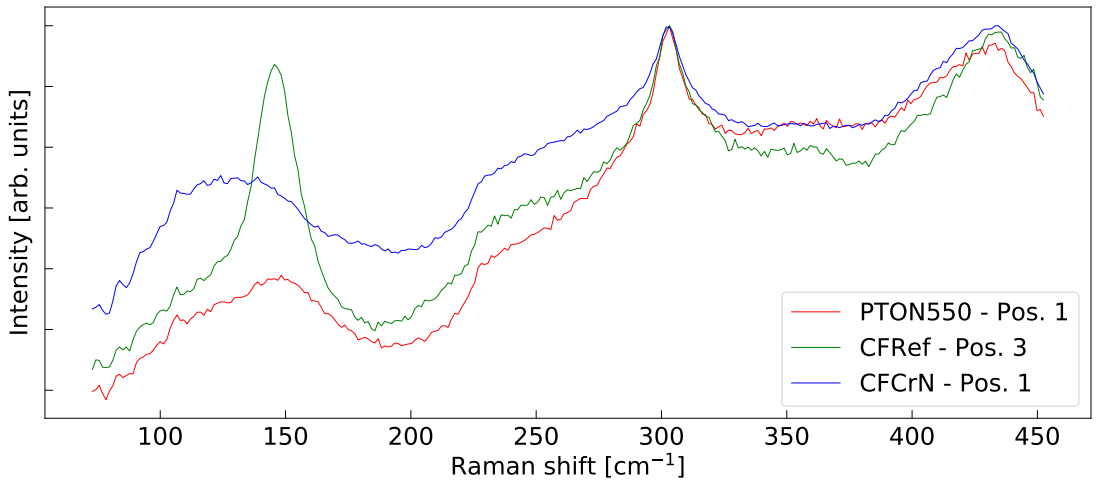

Figure 5.44: Raman spectra from lower spectrum scans of samples with amorphous structures.

CFRef still have a clear anatase peak, even compared to PTON550, which is somewhat unexpected. This sample was however deposited with more pulses in total, which could explain the more intense and distinct anatase peak. Both these spectra are from "plume centres" of TiO_2 deposited with background gas cycling between O_2 and N_2. In pos. 1 on the sample CFCrN, mostly TiO_2 was deposited with O_2 background gas. Still, it contains doping from the other "plume centre" of the sample, and thus shows signs of a more amorphous structure than both the on the other samples where they were deposited with gas cycling. This implies that the doping in pos. 1 of CFCrN was more damaging to the film, than the gas cycling without doping was to the crystallinity in the "plume centres" of the samples without doping.

Figure 5.45 show the upper scans from the same positions on the same samples as in figure 5.44. Here, the spectra are normalised against their shared peak around 612 cm^{-1}, that might be attributed to the dominant peak of rutile [26, 30, 31].

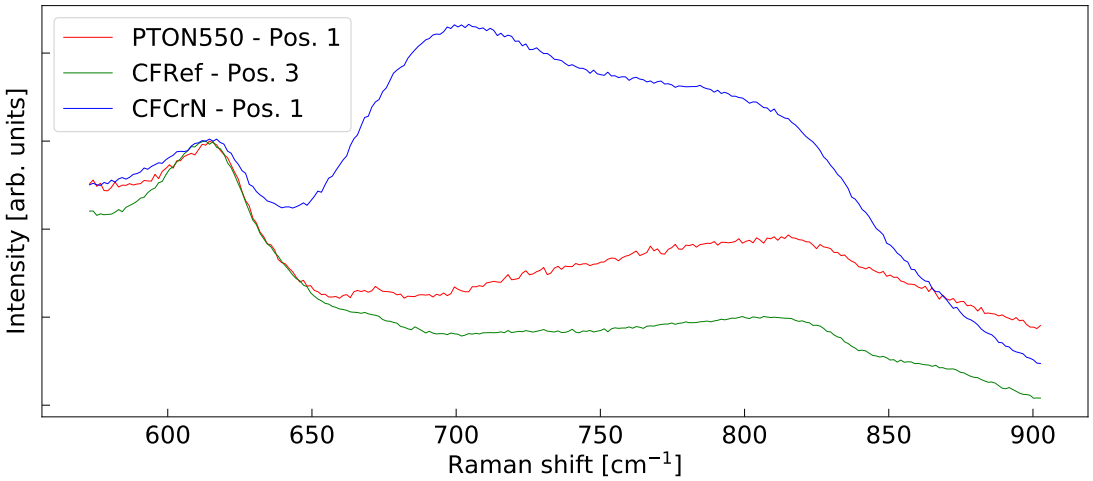

Figure 5.45: Raman spectra from upper spectrum scans of samples with amorphous structures.

From figure 5.45 it becomes apparent that CFCrN differs from the other two samples. As this is the only sample with doping, this difference is attributed to the doping.

5.12 Possible improvements and future work

The last sample CFCrN is the second one made with these parameters. The fluence is assumed to be equal between the two iterations, but as this thesis was written, this was not measured yet. One improvement would have been to also have conducted measurements on the original sample iteration.

As the measurements were conducted with a laser spot diameter on the micrometer order, it poses the question about how representative structure in the positions of measurement are for the overall structure of the film around the positions of measurement. If there are very local variations is the structure of the sample, say local crystalline grains in an overall amorphous structure, the measured spectrum would not fully represent this position on the sample if it was conducted directly on one of these grains. One improvement would be to conduct mapping around the positions to see how representative these positions are, and if there is a lot of variation around one position. If conducted on a sample with known nano-crystalline grains from other techniques, this could also give an account for the resolution of the Raman measurements.

For future work, a more detailed, quantitative analysis is proposed. Specifically, it would be interesting to study how the area under the obtained Raman peaks and their intensity correspond to the thickness of the film. There are examples of this in literature [38]. If possible, Raman could have the potential to be utilized as a

non-destructive way of measuring film thickness.

The samples studied were not processed in any way after deposition, to best study the effects of the PLD process. As it was shown that many of the deposition parameters was damaging to the crystallinity of the films, optimising these parameters for best possible crystallinity would be possible future work. It would also be interesting to anneal the already studied films, to see how this might better the damage crystallinity of the films.

6 Conclusion

Raman spectroscopy was used to characterise structure and crystallinity of TiO_2 based thin films, deposited using PLD, some of which were also deposited with background gas cycling between O_2 and N_2, and Cr-N co-doping. This revealed that anatase was the favoured crystal phase of the TiO_2 films when deposited with only O_2 background gas, while both deposition with N_2 background gas and doping proved to be extremely damaging for the crystallinity of the film, resulting in Raman spectra showing signs amorphous structures in the films. Smaller variations, like shifts in peak position and peak intensity was observed as results of both film thickness, as well as distance from the deposition plume centre. By using a micro-Raman setup, these variations was not only studied between the samples, but also locally and across the different samples.

Compared to the samples with high levels of crystallinity, the samples with amorphous structures proved difficult to gain detailed information from using Raman, as their spectra showed broadened and less distinctive peaks. Still, this provided useful results that helped characterise these films as amorphous.

It should be mentioned that Raman spectroscopy is generally considered a more qualitative than quantitative method, and was also largely treated this way during this thesis. There are however examples of more quantitative analysis methods applied to Raman data [25, 26], making it possible to analyse Raman data in greater detail than what fit the scope and capacity of this project. This is thus proposed for future work.

Bibliography

[1] Herman Solstrand. 'Surface characterization of TiO_2 based thin films'. Specialization project. Norwegian University of Science and Technology (NTNU), June 2021.

[2] 'April 25, 1954: Bell Labs Demonstrates the First Practical Silicon Solar Cell'. In: *APS News* 18.4 (Apr. 2009). American Physical Society. URL: https://www.aps.org/publications/apsnews/200904/physicshistory.cfm.

[3] Jenny Nelson. *The Physics Of Solar Cells*. Imperial College Press, 2003.

[4] Martin Green. *Third Generation Photovoltaics. Advanced Solar Energy Conversion*. Springer-Verlag Berlin Heidelberg, 2003.

[5] William Shockley and Hans J. Queisser. 'Detailed Balance Limit of Efficiency of p-n Junction Solar Cells'. In: *Journal of Applied Physics* 32.3 (1961), pp. 510–519. URL: https://doi.org/10.1063/1.1736034.

[6] A De Vos. 'Detailed balance limit of the efficiency of tandem solar cells'. In: *Journal of Physics D: Applied Physics* 13.5 (1980), pp. 839–846. URL: https://doi.org/10.1088/0022-3727/13/5/018.

[7] Fengcheng Wu et al. 'Quantum efficiency of intermediate-band solar cells based on non-compensated n-p codoped TiO2'. In: *The Journal of Chemical Physics* 137.10 (2012), p. 104702. URL: https://doi.org/10.1063/1.4750981.

[8] Alpa Dashora et al. 'Formation of an intermediate band in the energy gap of TiO2 by Cu–N-codoping: First principles study and experimental evidence'. In: *Solar Energy Materials and Solar Cells* 125 (2014), pp. 120–126. ISSN: 0927-0248. URL: https://doi.org/10.1016/j.solmat.2014.02.032.

[9] Qingsen Meng et al. 'Understanding electronic and optical properties of anatase TiO2 photocatalysts co-doped with nitrogen and transition metals'. In: *Phys. Chem. Chem. Phys.* 15.24 (2013), pp. 9549–9561. URL: https://doi.org/10.1039/C3CP51476E.

[10] C. Parks Cheney et al. 'Origins of Electronic Band Gap Reduction in Cr/N Codoped TiO_2'. In: *Phys. Rev. Lett.* 112.3 (Jan. 2014), p. 036404. URL: https://doi.org/10.1103/PhysRevLett.112.036404.

[11] Norbert Kaiser. 'Review of the fundamentals of thin-film growth'. In: *Appl. Opt.* 41.16 (2002), pp. 3053–3060. URL: https://doi.org/10.1364/AO.41.003053.

[12] C. Raman and K. Krishnan. 'The Negative Absorption of Radiation'. In: *Nature* 122 (1928), pp. 12–13. ISSN: 1364-0321. URL: https://doi.org/10.1038/122012b0.

[13] Andrew T. Young. 'Rayleigh scattering'. In: *Appl. Opt.* 20.4 (Feb. 1981), pp. 533–535. URL: https://doi.org/10.1364/AO.20.000533.

[14] Charles Kittel. *Introduction to Solid State Physics*. 8th ed. Wiley, 2005. ISBN: 0-471-41526X.

[15] Renishaw plc. *Raman spectroscopy explained*. Mar. 2017. URL: www.renishaw.com/raman.

[16] Komal Bapna, R.J. Choudhary and D.M. Phase. 'Evolution of different structural phases of TiO2 films with oxygen partial pressure and Fe doping and their electrical properties'. In: *Materials Research Bulletin* 47.8 (2012), pp. 2001–2007. ISSN: 0025-5408. URL: https://doi.org/10.1016/j.materresbull.2012.04.011.

[17] J.E.S. Haggerty et al. 'High-fraction brookite films from amorphous precursors'. In: *Sci Rep* 7 (2017), p. 15232. URL: https://doi.org/10.1038/s41598-017-15364-y.

[18] Masayuki Watanabe. 'Raman spectroscopy of charge-ordered states in Magnéli titanium oxides'. In: *physica status solidi c* 6.1 (2009), pp. 260–263. URL: https://doi.org/10.1002/pssc.200879898.

[19] C Langlade et al. 'Characterization of titanium oxide films with Magnéli structure elaborated by a sol–gel route'. In: *Applied Surface Science* 186.1 (2002), pp. 145–149. ISSN: 0169-4332. URL: https://doi.org/10.1016/S0169-4332(01)00642-0.

[20] A Barata, L Cunha and C Moura. 'Characterisation of chromium nitride films produced by PVD techniques'. In: *Thin Solid Films* 398-399 (2001). Proceedings of the 28th International Conference on Metallurgic Coatings and Thin Films, pp. 501–506. ISSN: 0040-6090. URL: https://doi.org/10.1016/S0040-6090(01)01498-5.

[21] Luca Bindi et al. 'Kishonite, VH2, and Oreillyite, Cr2N, Two New Minerals from the Corundum Xenocrysts of Mt Carmel, Northern Israel'. In: *Minerals* 10.12 (2020). ISSN: 2075-163X. URL: https://doi.org/10.3390/min10121118.

[22] Sa Li and P. Jena. 'Origin of the anatase to rutile conversion of metal-doped TiO_2'. In: *Phys. Rev. B* 79.20 (May 2009), p. 201204. URL: https://doi.org/10.1103/PhysRevB.79.201204.

[23] Matthew D. Sonntag et al. 'Recent Advances in Tip-Enhanced Raman Spectroscopy'. In: *The Journal of Physical Chemistry Letters* 5.18 (2014). PMID: 26276323, pp. 3125–3130. URL: https://doi.org/10.1021/jz5015746.

[24] David Tuschel. 'Why Are the Raman Spectra of Crystalline and Amorphous Solids Different?' In: *Spectroscopy* 32.3 (2017), pp. 26–33. URL: https://www.spectroscopyonline.com/view/why-are-raman-spectra-crystalline-and-amorphous-solids-different.

[25] B. Güttler et al. 'Quantitative evaluation of the oxygen content in $YBa_2Cu_3O_{7-\delta}$ epitaxially grown thin films using near-infrared excited Raman spectrometry'. In: *Physica C: Superconductivity* 251.1 (1995), pp. 165–170. ISSN: 0921-4534. URL: https://doi.org/10.1016/0921-4534(95)00405-X.

[26] Sebastian Schipporeit and Dieter Mergel. 'Spectral decomposition of Raman spectra of mixed-phase TiO2 thin films on Si and silicate substrates'. In: *Journal of Raman Spectroscopy* 49.7 (2018), pp. 1217–1229. URL: https://doi.org/10.1002/jrs.5369.

[27] Qiu Li et al. 'Study on Local Residual Stress in a Nanocrystalline Cr2O3 Coating by Micro-Raman Spectroscopy'. In: *Coatings* 9.8 (2019). ISSN: 2079-6412. URL: https://doi.org/10.3390/coatings9080500.

[28] Lafuente B et al. 'The power of databases: the RRUFF project.' In: *Highlights in Mineralogical Crystallography*. Ed. by T Armbruster and R M Danisi. Berlin, Germany: W. De Gruyter, 2015, pp. 1–30. URL: https://rruff.info/.

[29] N. Stavrias, P.G. Spizzirri and S. Prawer. 'Electronic Raman scattering as a probe for investigating interactions between impurities in silicon'. In: *Journal of Raman Spectroscopy* 50.4 (2019), pp. 595–602. URL: https://doi.org/10.1002/jrs.5543.

[30] Ibrahim A. Alhomoudi and G. Newaz. 'Residual stresses and Raman shift relation in anatase TiO2 thin film'. In: *Thin Solid Films* 517.15 (2009), pp. 4372–4378. ISSN: 0040-6090. URL: https://doi.org/10.1016/j.tsf.2009.02.141.

[31] F. Rossella et al. 'TiO2 thin films for spintronics application: a Raman study'. In: *Journal of Raman Spectroscopy* 41.5 (2010), pp. 558–565. URL: https://doi.org/10.1002/jrs.2465.

[32] Bhagaban Kisan et al. 'Size and strain induced phase formation and ferromagnetism in reduced TiO2 powders'. In: *Journal of Physics and Chemistry of Solids* 154 (2021), p. 110058. ISSN: 0022-3697. URL: https://doi.org/10.1016/j.jpcs.2021.110058.

[33] Mohd Arif, Amit Sanger and Arun Singh. 'Sputter deposited chromium nitride thin electrodes for supercapacitor applications'. In: *Materials Letters* 220 (2018), pp. 213–217. ISSN: 0167-577X. URL: https://doi.org/10.1016/j.matlet.2018.02.094.

[34] Yagyanidhi Tripathi et al. 'Study of phase formulation in CrN thin films and its response to a minuscule oxygen flow in reactive sputtering process'. In: *Thin Solid Films* 670 (2019), pp. 113–121. ISSN: 0040-6090. URL: https://doi.org/10.1016/j.tsf.2018.10.009.

[35] Shankar Dutta et al. 'Growth and characterization of ultrathin TiO2-Cr2O3 nanocomposite films'. In: *Journal of Alloys and Compounds* 696 (2017), pp. 376–381. ISSN: 0925-8388. URL: https://doi.org/10.1016/j.jallcom.2016.11.284.

[36] V. R. Akshay et al. 'Visible range optical absorption, Urbach energy estimation and paramagnetic response in Cr-doped TiO2 nanocrystals derived by a sol–gel method'. In: *Phys. Chem. Chem. Phys.* 21.24 (2019), pp. 12991–13004. URL: https://doi.org/10.1039/C9CP01351B.

[37] V. Sammelselg et al. 'Structural characterization of TiO2–Cr2O3 nanolaminates grown by atomic layer deposition'. In: *Surface and Coatings Technology* 204.12 (2010). Proceedings of the European Materials Research Socierty (E-MRS) Spring Meeting 2009, pp. 2015–2018. ISSN: 0257-8972. URL: https://doi.org/10.1016/j.surfcoat.2009.11.039.

[38] Xabier Rodríguez-Martínez et al. 'Quantifying local thickness and composition in thin films of organic photovoltaic blends by Raman scattering'. In: *J. Mater. Chem. C* 5.29 (2017), pp. 7270–7282. URL: https://doi.org/10.1039/C7TC01472D.

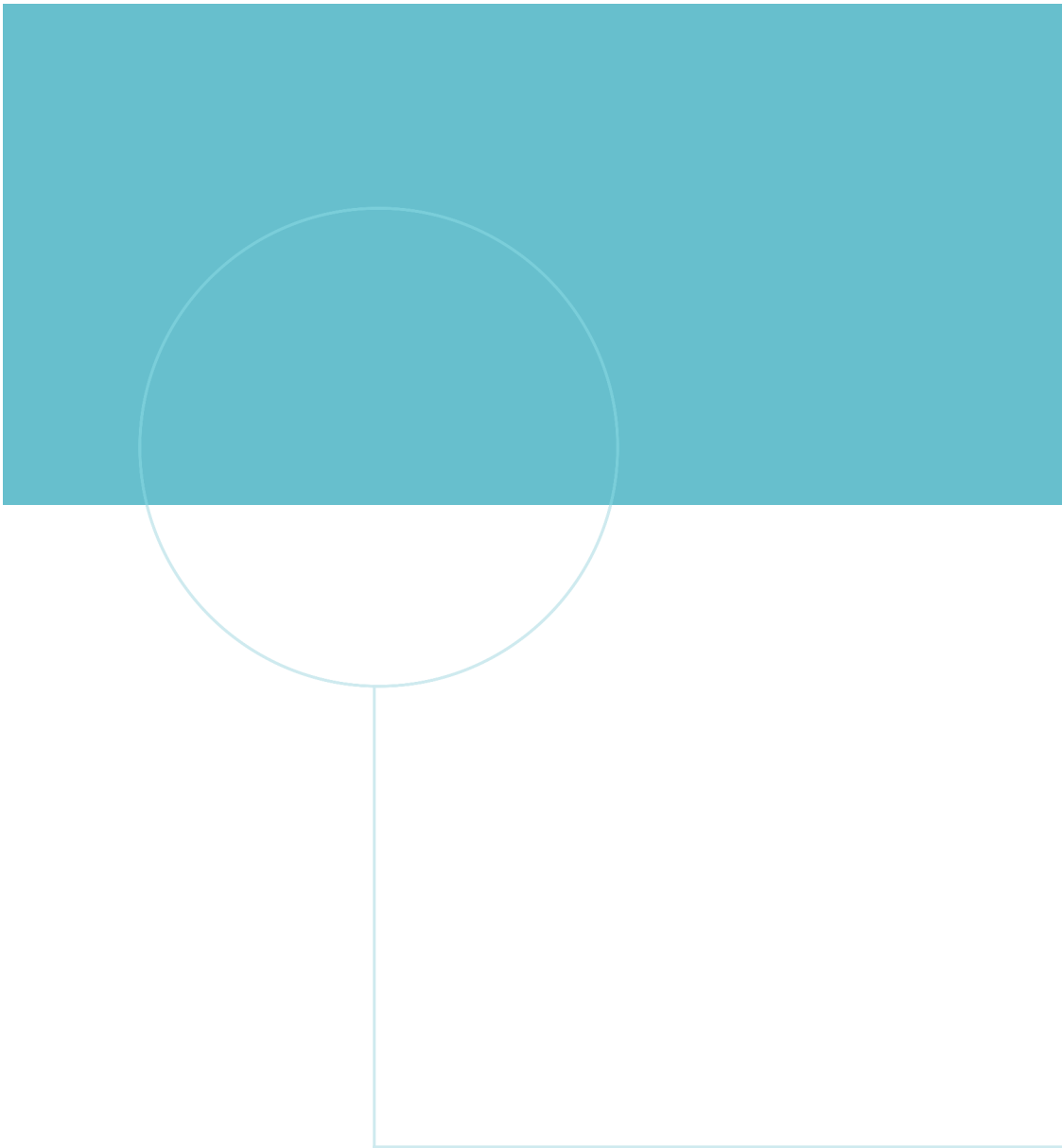

NTNU

Norwegian University of
Science and Technology